FULL PAPER

From ambient vibration data analysis to 1D ground-motion prediction of the Mj 5.9 and the Mj 6.5 Kumamoto earthquakes in the Kumamoto alluvial plain, Japan

Salomon Hailemikael[1*], Giuseppe Di Giulio[2], Giuliano Milana[1], Maurizio Vassallo[2] and Paola Bordoni[1]

Abstract

We present horizontal ground motion predictions at a soft site in the Kumamoto alluvial plain for the Mj 5.9 and Mj 6.5 Kumamoto earthquakes of April 2016, in the framework of an international blind prediction exercise. Such predictions were obtained by leveraging all available information which included: (i) analysis of earthquake ground motions; (ii) processing of ambient vibration data (AMV); and (iii) 1D ground response analysis. Spectral analysis of earthquake ground-motion data were used to obtain empirical estimates of the prediction site amplification function, with evidence of an amplification peak at about 1.2 Hz. Horizontal-to-vertical spectral ratio analysis of AMV confirmed this resonance frequency and pointed out also a low-frequency resonance around 0.3 Hz at the prediction site. AMV were then processed by cross-correlation, modified spatial autocorrelation and high-resolution beamforming methods to retrieve the 1D shear-wave velocity (Vs) structure at the prediction site by joint inversion of surface-wave dispersion and ellipticity curves. The use of low frequency dispersion curve and ellipticity data allowed to retrieve a reference Vs profile down to few thousand meters depth which was then used to perform 1D equivalent-linear simulations of the M 5.9 event, and both equivalent-linear and nonlinear simulations of the M 6.5 event at the target site. Adopting quantitative goodness-of-fit metrics based on time–frequency representation of the signals, we obtained fair-to-good agreement between 1D predictions and observations for the Mj 6.5 earthquake and a poor agreement for the Mj 5.9 earthquake. In terms of acceleration response spectra, while ground-motion overpredictions were obtained for the Mj 5.9 event, simulated ground motions for the Mj 6.5 earthquake severely underestimate the observations, especially those obtained by the nonlinear approach.

Keywords Ambient vibration, Surface-wave dispersion, 1D ground response analysis, ESG6 blind test, Kumamoto earthquake sequence
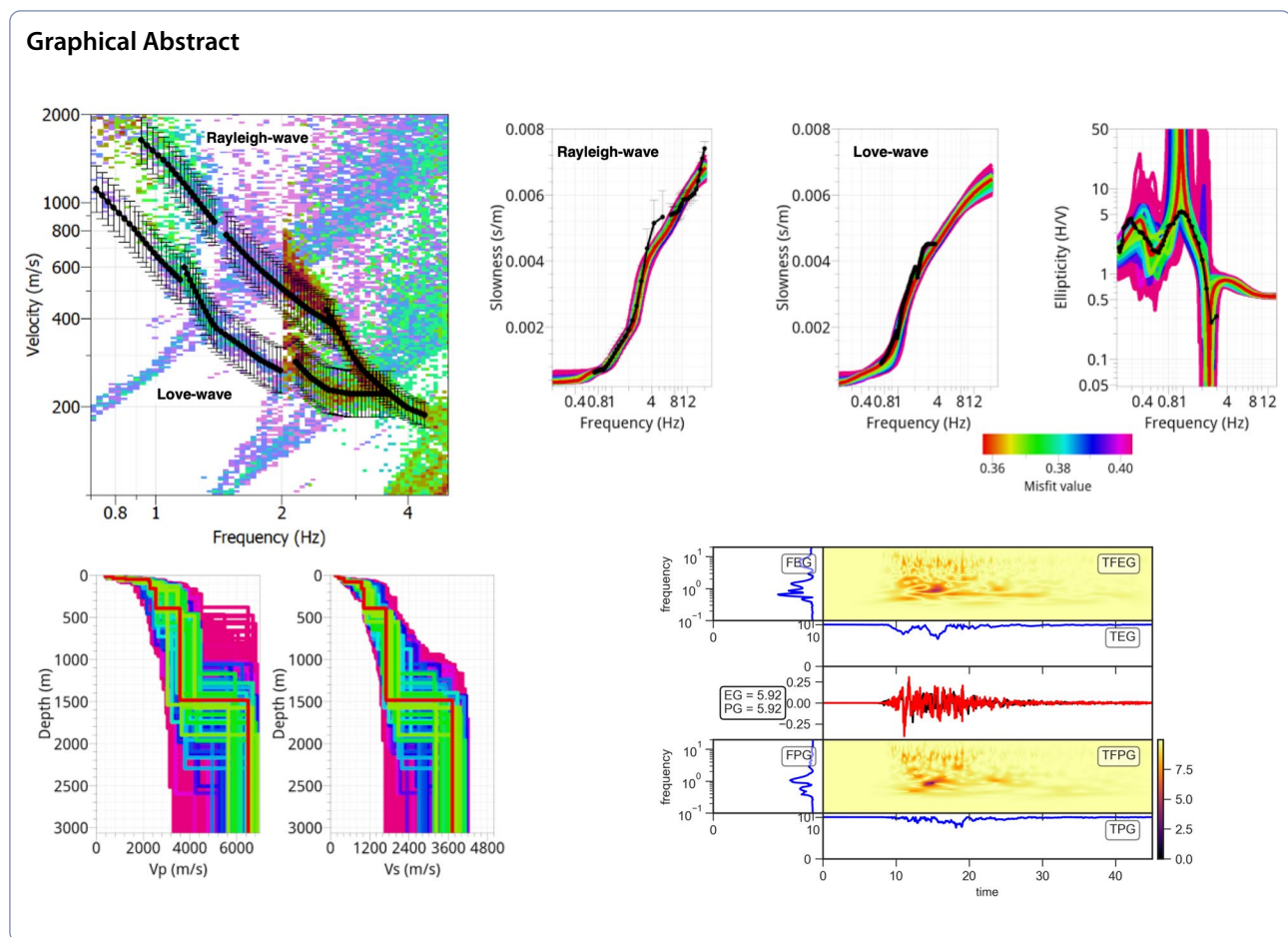
*Correspondence:
Salomon Hailemikael
salomon.hailemikael@ingv.it
Full list of author information is available at the end of the article

Hailemikael *et al. Earth, Planets and Space*　　(2023) 75:105

Page 2 of 25

Graphical Abstract

Introduction

The assessment of our capability of predicting earthquake ground motion is of paramount importance for performance-based design and retrofitting of existing building stock. Moreover, earthquake risk mitigation strategies also rely on the capability of earth scientists and earthquake engineers to predict the ground motion at a site of interest (Chaljub et al 2015). Such importance have stimulated the research on this field, with particular emphasis on the determination of the earthquake source characteristics (Galvez et al 2014), the development of methods for the reconstruction of realistic 3D subsurface structures (Di Michele et al 2022) and the implementation of efficient and accurate computational methods for ground motion estimation (Bielak et al 2010), including the nonlinear behavior of shallow geologic materials (Esmaeilzadeh et al 2019, to name a few).

A relatively long tradition of ground motion prediction assessment has been established in the framework of IASPEI/IAEE international symposia on the Effects of Surface Geology (ESG) on Seismic Motion; in these conferences, such as Odawara, Japan (1992), Yokohama, Japan (1998) and Grenoble, France (2006), several blind prediction exercises were devoted to test geophysical methods for retrieving realistic models of the subsurface and verify the accuracy of computational methods in reproducing real earthquake ground motion in complex settings (Chaljub et al. 2010).

Following this tradition, the more recent ESG6, held in Kyoto, Japan, in 2021, promoted a similar international blind prediction exercise with the aim of evaluating the capability of expert researchers to retrieve a realistic 1D shear-wave velocity (Vs) structure from seismic surveys performed at a prediction site in the Kumamoto plain (Step 1; Matsushima et al., submitted to Earth Planets and Space; Chimoto et al. 2023). This target site recorded seismic events of the 2016 Kumamoto sequence, and the blind exercise (Tsuno et al., submitted to Earth Planets and Space) further investigated the accuracy in reproducing weak- (Step 2) and strong- (Step 3) ground motions belonging to the sequence by both empirically based and numerical methods.

It is well known that ground motion amplification at a site is controlled by seismic wave propagation, particularly close to the surface, therefore the knowledge

Hailemikael *et al. Earth, Planets and Space*   (2023) 75:105

Page 3 of 25

of the Vs subsurface structure is an essential element for ground response analysis (Kramer 1996; Boore 2004). Vs structure at a site can be obtained by both invasive and non-invasive methods; while the former were usually considered more reliable due to their processing simplicity, the latter have gained increasing popularity due to their cost-effectiveness (Bard et al. 2010; Garofalo et al. 2016a). In fact, invasive methods, such as down-hole or cross-hole tests, imply moderate-cost operations and logistic difficulties due to the need of borehole drillings. Whereas passive non-invasive methods, which are based on surface-wave propagation analysis (Foti et al. 2014), require as easy and low-cost field operations as deploying standard seismic instrumentation on the surface in a predetermined 2D geometry (Maranò et al. 2014). Moreover, non-invasive approaches allow to investigate, even if with lower accuracy, the deeper part of soil columns. However, these advantages are countered by complex and time-consuming processing and inversion of the acquired data.

More in detail, several processing methods were proposed to retrieve Rayleigh and Love-wave dispersion curve (DC) from ambient vibrations (Aki 1957; Capon 1969; Tokimatsu 1997; Bettig et al. 2001; Ohori et al. 2002; Shapiro and Campillo 2004; Okada 2006; Maranò et al. 2017; Wathelet et al. 2018; Vassallo et al. 2019). Several approaches were proposed as well for the inversion of DC data to obtain the Vs profile at the investigated site (Herrmann 1987; Yamanaka and Ishida 1996; Wathelet 2008). This last step of analysis is characterized by high non-linearity and non-uniqueness of the solution (Foti et al. 2009; Renalier et al. 2010; Boaga et al. 2011; Di Giulio et al. 2012; Gosselin et al. 2022) which affects the output of a ground response analysis (GRA). The significant expertise required by passive surface wave methods promoted the development of projects and international initiatives devoted to the advancement of the current state-of-practice (Bard et al. 2010; Garofalo et al. 2016a, 2016b).

A general limitation on the use of passive surface-wave methods is their formal applicability to 1D site conditions, namely subsurface structures which can be approximated to a stack of homogeneous isotropic horizontal viscoelastic layers overlying an elastic half-space. An approach for the practical verification of such conditions could be performing horizontal-to-vertical spectral ratio (H/V) analysis (Nogoshi and Igarashi 1971; Nakamura 1989; SESAME 2005) of the data acquired by a 2D array of seismic sensors. In case of homogeneous results in terms of H/V curves across the 2D array, the 1D condition may be reasonably assumed for the investigated site. In addition, H/V data represent also a valuable support for Vs profile

retrieval due to their relation with Rayleigh-wave ellipticity data (Fäh et al. 2003, 2009; Hobiger et al. 2009), which can be used as a joint-inversion target along with DC data (Hobiger et al. 2013; Marcucci et al. 2019). Under the 1D site approximation, the analysis of seismic wave propagation can be reduced to that of vertically propagating horizontally polarized shear-wave (SH) through horizontal soil layering from a transmitting half-space boundary at the bottom of the 1D soil column (Kramer 1996). This assumption is at the foundation of 1D GRA, which allows for the prediction of surface ground motion based on the availability of a representative bedrock ground motion input, realistic Vs vertical profile at the site, a mass density profile and a description of the soil constitutive model. In particular, recent studies focused on the comparison between linear, equivalent-linear (EQL) and nonlinear (NL) soil behavior with observations (see Kaklamanos and Bradley 2018 for a comprehensive review).

Regarding the relation between input ground motion level and soil constitutive model, it was found that the commonly adopted EQL fails in reproducing observations if the maximum shear strain induced by the input earthquake excitation in the soil exceeds some threshold level, estimated to be in the range 0.2–0.3% (Kim and Hashash 2013; Yee et al. 2013). Therefore, NL ground simulations are recommended in case of strong ground motions (Stewart et al. 2014).

Studies also addressed the issue of the applicability of 1D GRA given that it cannot take into account complex 2D and 3D subsurface structures which severely affects seismic wave propagation in valleys and basins (Aki and Larner 1970; Bard and Bouchon 1985). Experimental validation of the 1D assumption is indeed a difficult task which can be tackled by different approaches (Pilz and Cotton 2019). This could explain the large variability of the percentage of sites in a given sample for which the 1D assumption holds, ranging from 16% (Thompson et al. 2012) to 69% (Tao and Rathje 2020), that was estimated by several studies based on different comparison criteria between 1D GRA results and ground motion observations.

In this paper, we describe and discuss the ground motion predictions obtained for two events of the Kumamoto seismic sequence which occurred in southwest Japan in 2016 and culminated with the April 15th Mj 7.3 mainshock. In particular, we focused on the largest aftershock (Mj 5.9, Step 2) of the Kumamoto earthquake sequence and the April 14th, 2016 foreshock (Mj 6.5, Step 3) at the prediction site (KUMA) by: i) the estimation of the 1D Vs structure at the prediction site by processing of ambient vibration (AMV) data recorded by 2D seismic arrays; and ii) numerical simulation of earthquake

Hailemikael *et al. Earth, Planets and Space*   (2023) 75:105

Page 4 of 25

strong- and weak-motions by 1D ground response analysis (GRA).

The aim is to quantitatively compare the recordings of the two Kumamoto earthquakes (Mj 5.9 and Mj 6.5) with the predictions obtained by current state-of-practice in earthquake engineering, which include building a large depth 1D Vs model from advanced processing of AMV data acquired by several 2D arrays of different aperture (Step 1; Matsushima et al., submitted to Earth Planets and Space; Chimoto et al. 2023), and performing 1D GRA adopting EQL and NL constitutive models (Steps 2 and 3; Tsuno et al., submitted to Earth Planets and Space). The paper is organized as follows: after a brief description of the available data (Matsushima et al., submitted to Earth Planets and Space), we describe the H/V analysis of AMV data carried out to evaluate the feasibility of the 1D assumption for the site and obtain information on Rayleigh-wave ellipticity. Then, we describe the results of the processing methods adopted for the wide frequency band DC data retrieval, which include Modified Spatial Autocorrelation (MSPAC, Bettig et al. 2001), cross-correlation (Shapiro and Campillo 2004) and high-resolution Rayleigh-wave three-component beam forming (RTBF, Wathelet et al. 2018). Subsequently, the procedures for the joint-inversion of DC and ellipticity

data are described and the results in terms of Vs profile are illustrated (Step 1; Chimoto et al. 2023). Finally, we depict the 1D GRA predictions obtained for Steps 2 and 3 (Mj 5.9 and 6.5, respectively) and compare these with the observed ground motions at the KUMA site.

Geological setting and available data

The prediction site, KUMA, is located in the N sector of the Kumamoto plain in the Kumamoto prefecture, Japan (Fig. 1a). In its easternmost sector facing the Ariake bay, this plain has a width of roughly 9000 m in the NS direction and it is filled by alluvial deposits of the Shirakawa and Midorikawa rivers and by volcano-clastic deposits from the Aso volcano (Tsuno et al. 2017). Previous 2D geophysical surveys (MEXT, 2016) inferred that the alluvial and volcano-clastic layered units have a total thickness of roughly 500 m, while a deep seismic discontinuity is present down to a maximum depth of roughly 1500 m in the N part of the basin. The northern margin of the basin is limited by a south dipping fault which separates the layered sedimentary units from the andesite rocks of Mt. Kinbo outcropping northward. In the Mt. Kinbo area a reference recording site, SEVO, is located (Fig. 1a). Information about the deep P-wave velocity (Vp), Vs and density vertical structures in the area is also available from
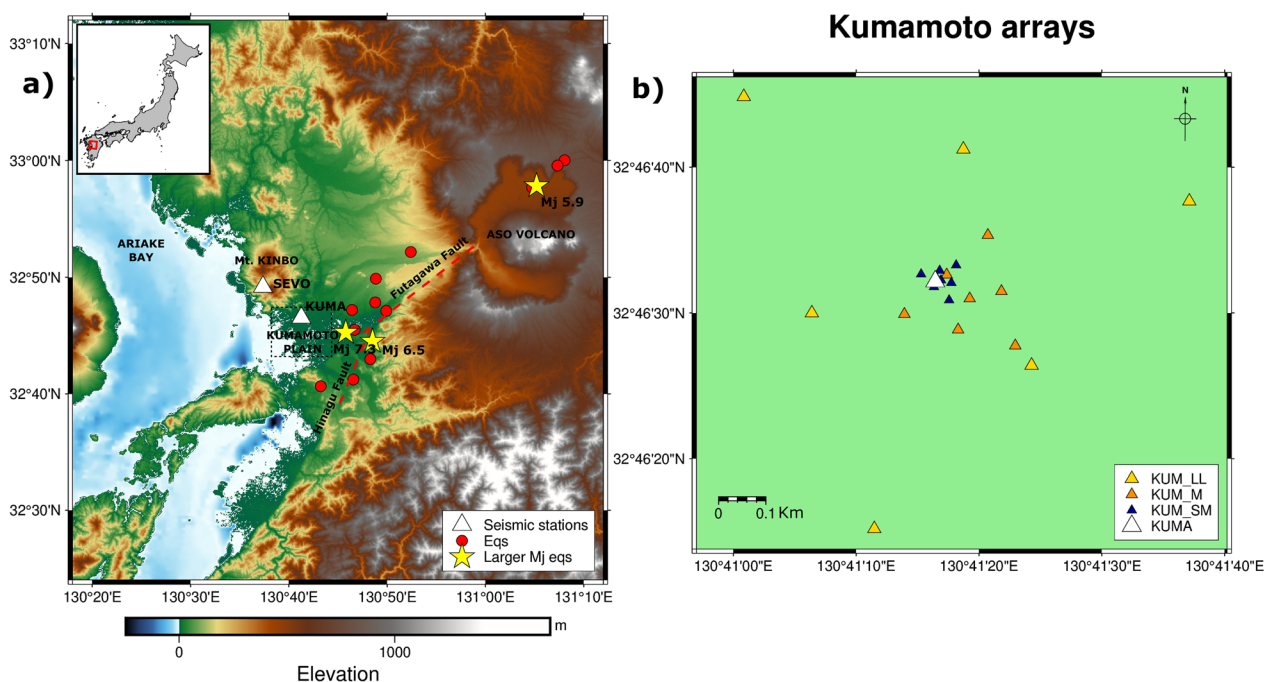
Fig. 1 Map showing the location of the prediction KUMA and reference SEVO sites (**a**) and 2D arrays geometry (**b**). Panel a: distribution of earthquakes belonging to the Kumamoto sequence for which recordings at the sites are available (red circles). The epicenter of the Mj 5.9 (Step 2) aftershock and the Mj 6.5 (Step 3) and Mj 7.3 mainshocks are shown as yellow stars. Panel b: deployment geometry for the KUM-LL, KUM-M and KUM-SM arrays around the prediction site KUMA (Kumamoto plain). KUM-SS1 and KUM-S arrays have similar geometry but are not visible at the scale of the image due to their lower aperture (side lengths of the larger triangular geometry of about 20 m for KUM-S and 2 m for KUM-SS1)

the Japan Integrated Velocity Structure Model (JIVSM, Koketsu et al. 2012) and the Japan Seismic Hazard Information System (J-SHIS ver.2, NIED). Both models show discontinuities in all parameter vertical profiles at depths between 400 and 600 m, which well correlate with the estimated thickness of the alluvial and volcano-clastic filling of the Kumamoto plain (Fig. 2 c,d). In particular, the J-SHIS model shows a sharp increase in Vp and Vs at about 450 m depth, where Vp varies from 2600 m/s to 5000 m/s and Vs from 1200 m/s to 2600 m/s (dotted lines in Fig. 2,c). Only the JIVSM model highlights a large Vs and Vp discontinuity at about 1450 m depth, roughly corresponding with the estimated basin maximum depth (MEXT, 2016), where Vp varies from 4200 m/s to 5600 m/s and Vs from 2400 to 3200 m/s (solid lines in Fig. 2,c).

The prediction site KUMA and the reference site SEVO (Matsushima et al., submitted to Earth Planets and Space), were equipped with a strong-motion sensor and a seismic sensor, respectively. These stations recorded several ground motions of the 2016 Kumamoto seismic sequence (Table 1), including the 14th April 2016 Mj 6.5 foreshock and the April 15th Mj 7.3 mainshock. The foreshock was caused by right-lateral strike-slip faulting along the Hinagu fault while the mainshock started from a Northern slip patch of this same fault and transferred to the Futagawa fault to the NE (Fig. 1a), where also a significant normal slip component was observed (Asano and Iwata 2016). Among those waveforms, we focused on the Mj 6.5 foreshock (Step 3) and the largest aftershock (Mj 5.9, Step 2) of the sequence (Fig. 1a and Table 1). We neglected the Mj 7.3 mainshock ground-motions because the recording is incomplete due to a system malfunctioning at the KUMA site instrument.

For the passive analysis, the AMV data consist of 3-component recordings acquired by seismic sensors (fundamental period equal to 10 s) connected to high-resolution data loggers (24-bit dynamic range) and deployed in 2-D array configuration around KUMA site. The 5 arrays (KUM-SS1, KUM-S, KUM-SM, KUM-M and KUM-LL) considered in the blind prediction have nested triangular geometry (Fig. 1b) with increasing aperture (larger side of the triangle ranging from about 2 m to 960 m), therefore allowing for surface wave dispersion retrieval in a wide range of frequencies. Each array is made of 7 sensors with a central station. The recording length is 45 min for KUM-SS1, 1 h for KUM-S and 2 h for the remaining arrays; recording sampling frequency is 200 Hz for all signals. Given the short aperture of the smallest array which severely limits its investigated frequency bandwidth, recordings from the SS1 array were only used for single-station analysis. Due to a system malfunction in the NS component of the central sensor (station 1) in common with all arrays, data acquired by

this sensor were discarded from the processing method which required all three-component (3C) recordings at each sensor for DC retrieval (three-component Rayleigh Beam Forming—RTBF, see "Vs-profile retrieval from AMV data" Section for further details). But data from the central station were included in the remaining analyses which focus only on the vertical component of motion.

The description of the finer structure of the basin infilling and the geotechnical parameters of the investigated soils at the KUMA site were obtained by passive geophysical measurements (Chimoto et al. 2016) and geotechnical investigations, including borehole stratigraphic log, Vp and Vs profiles from PS logging and laboratory testing (Fig. 2a; OYO 2020). Laboratory tests, including cyclic triaxial testing, were carried out on 5 samples (T1–T5) collected at different depths (from 4 to 23 m) to estimate physical and nonlinear properties of the soils which we included in our 1D modeling. The shallower 30 m are mainly composed of sands, below which an 8-m-thick gravel layer is found. At the bottom of the borehole, around 40 m depth, the stratigraphic log reports the presence of tuff breccia (Fig. 2a). The shallower velocity profile shows Vs values lower than 200 m/s down to 20 m depth (solid red line in Fig. 2a). Such values are in agreement with the estimated Vs from passive geophysical measurements (dotted red line in Fig. 2a; Chimoto et al. 2016). Then the Vs values gradually increase to 420 m/s in correspondence of the tuff deposits.

Data analysis
Empirical amplification function at KUMA by earthquake data analysis

The earthquake ground motions (Table 1) recorded at the predictions site KUMA, located on soft and deep alluvial deposits, and at the reference site SEVO, located on andesite rock of Mt. Kinbo, were processed by means of spectral analysis to obtain empirical estimates of the KUMA site amplification functions. To this aim, we employed the well known horizontal-to-vertical spectral ratio (EHV, Field and Jacob 1995) and standard spectral ratio (SSR; Borcherdt 1994) methods, both of which are considered to provide robust estimates of the investigated site amplification function. SSR method relies on the identification of a reference recording site (Steidl et al. 1996), usually located on rock or firm soil, for which site effects could be considered negligible. Under the conditions of (i) close site-to-reference distance (Rref) with respect to the site epicentral distance (Rd, such that $Rref < < Rd/5$) and ii) sufficient signal-to-noise ratio of the recordings obtained at both stations (SNR > 3), the SSR estimates can be obtained by calculating the ratio between Fourier amplitude spectra (FAS) of soft site and reference station as:

Hailemikael *et al. Earth, Planets and Space*   (2023) 75:105

Page 6 of 25
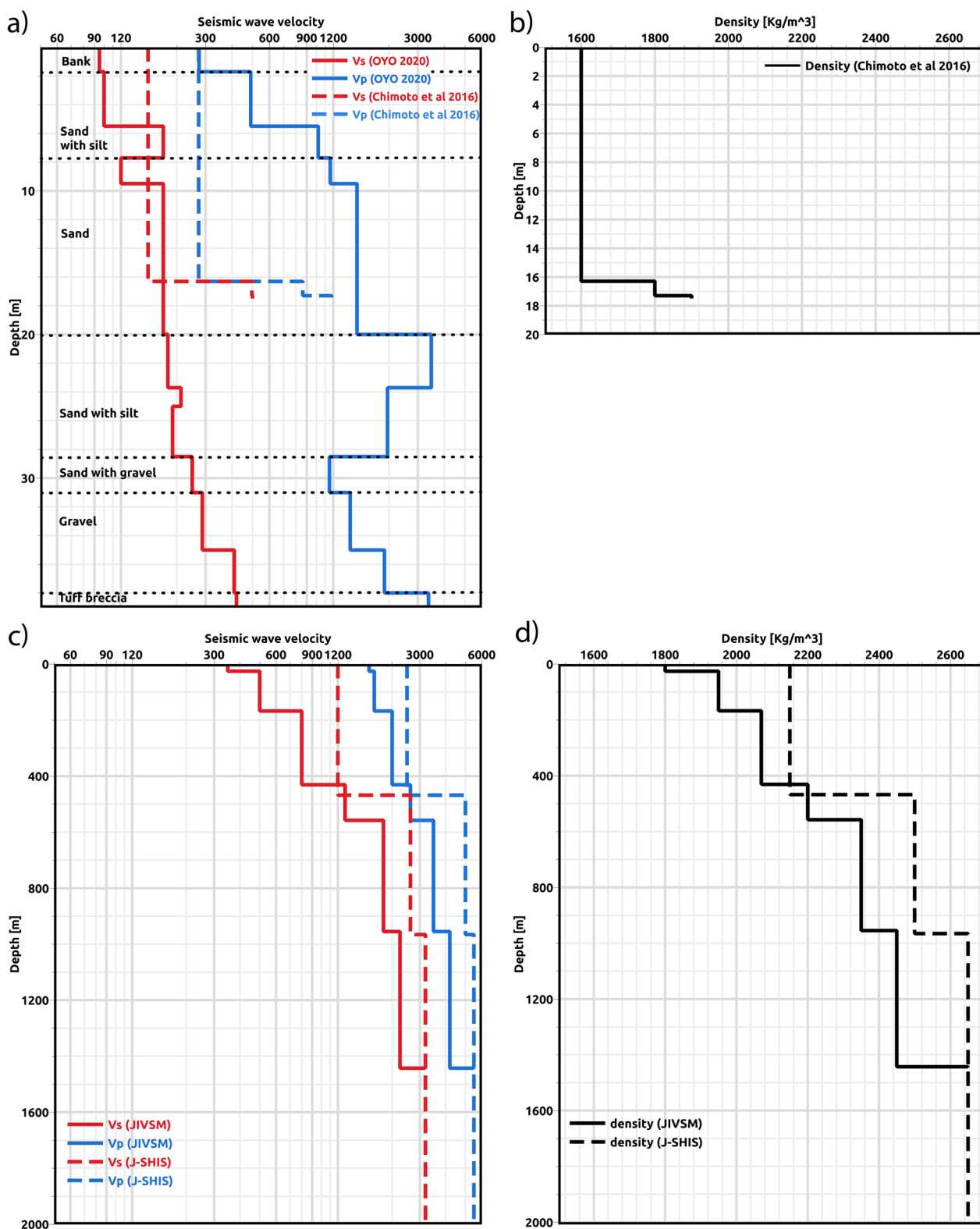
Fig. 2 a Shallow Vp and Vs models obtained from PS logging (OYO 2020) and from passive geophysical measurements (Chimoto et al. 2016). The horizontal dotted lines show the subdivision between the main shallow geological units from geotechnical investigation (OYO 2020). **b** Shallow density model by Chimoto et al. (2016). **c** Vp, Vs and density (**d**) vertical structures from the Japan Integrated Velocity Structure Model (JIVSM, Koketsu et al. 2012) and the Japan Seismic Hazard Information System by (J-SHIS ver.2, NIED)

Hailemikael *et al. Earth, Planets and Space*   (2023) 75:105

Page 7 of 25

Table 1 List of earthquakes for which recordings are available at the prediction KUMA and reference SEVO sites

ID	YY	MM	DD	HH	min	ss	Lat. (degree)	Long. (degree)	Depth (km)	Mj
01	**2016**	**04**	**14**	**21**	**26**	**34.43**	**32.7417**	**130.8087**	**11.39**	**6.5**
02	2016	04	16	01	05	42.48	32.7163	130.8048	15.46	3.3
03	2016	04	16	01	25	05.47	32.7545	130.7630	12.45	7.3
04	**2016**	**04**	**16**	**03**	**03**	**10.78**	**32.9638**	**131.0868**	**06.89**	**5.9**
05	2016	04	16	04	05	49.20	32.7973	130.8132	12.29	4.0
06	2016	04	16	07	23	54.32	32.7867	130.7738	11.93	4.8
07	2016	04	16	11	02	51.71	32.7583	130.7782	14.57	4.4
08	2016	04	17	00	14	51.69	32.9617	131.0792	08.92	4.8
09	2016	04	17	04	46	49.09	32.6872	130.7762	10.32	4.5
10	2016	04	17	19	23	41.22	32.6775	130.7207	10.58	4.4
11	2016	04	18	08	35	43.02	32.8695	130.8733	10.2	4.2
12	2016	04	21	21	52	3.39	32.7853	130.8318	10.98	4.0
13	2016	05	05	10	31	30.47	33.0003	131.1342	11.16	4.6
14	2016	05	05	10	40	12.83	32.9928	131.1222	10.81	4.9
15	2016	05	19	02	37	44.28	32.8313	130.8142	16.43	3.9

Origin time (year, month, day, hour, minute and seconds), position (latitude, longitude, depth) and magnitude are listed. The strong- and weak earthquake ground motions considered in step 2 (ID#04) and step 3 (ID#01) of the ESG6 are reported in bold

$$SSR = \frac{FAS_{site}}{FAS_{reference}}.$$

Since a reference site is not always available, the EHV method has been proposed which consist in the ratio between the FAS of the horizontal earthquake ground motion and the FAS of vertical component at the same site:

$$EHV = \frac{FAS_{horizontal}}{FAS_{vertical}}.$$

EHV method assumes that the vertical component of ground motions is not affected by site effects; however, it has been proved that this hypothesis is often not verified in real data (Felicetta et al. 2021) and, therefore, the EHV could be considered as a lower boundary of the site amplification level with respect to the SSR method. In any case, both SSR and EHV can provide consistent and robust estimates of the investigated site fundamental resonance frequency (Pilz et al. 2009).

Calculation of SSR and EHV includes common processing steps, like removal of the DC component and detrending before tapering and conversion to the frequency domain. The earthquake velocity records acquired at SEVO station were differentiated to obtain acceleration records before computation of FAS. Horizontal FAS were calculated for each station as geometric average of NS and EW components of ground motions. Then, the average SSR and EHV estimates from all earthquake records were calculated assuming lognormal distribution of FAS amplitudes.

The SSR empirical amplification function at KUMA, and EHVs calculated for both prediction KUMA and reference SEVO stations using the signals originated by the 12 earthquakes with Mj < 5 listed in Table 1 are reported in Fig. 3. The EHV function calculated at the reference SEVO site shows maximum value around 0.4 Hz, with amplitude around value 3.5, a secondary maximum around 1.2 Hz and average amplitude below 2.5 for frequencies larger than 1 Hz (Fig. 3, top panel). This result suggests that this site is likely affected by a low-frequency amplification (< 1 Hz) and could be considered a good reference in the higher frequency band. The EHV calculated at KUMA evidenced a clear amplification peak around 1.2 Hz, with average amplitude around 6 and a secondary maximum around 2 Hz (Fig. 3, middle panel). The SSR function at KUMA presented maxima at 1.2 and 7 Hz, with similar average amplitude around 8, and at 2.5 Hz, with slightly lower amplitude. The comparison between the two site amplification function estimation methods allowed us to identify the site fundamental resonance frequency at Kuma, which is around 1.2 Hz. A dubitative peak is also suggested in the low frequency part (around 0.4–0.5 Hz) but not well resolved by the SSR analysis.

H/V spectral ratios of AMV and Rayleigh-wave ellipticity retrieval

AMV data were analyzed by computing the H/V spectral ratios to evaluate the degree of homogeneity in the subsurface conditions below each array. We used the Geopsy code (Wathelet et al. 2020) using a running time-window
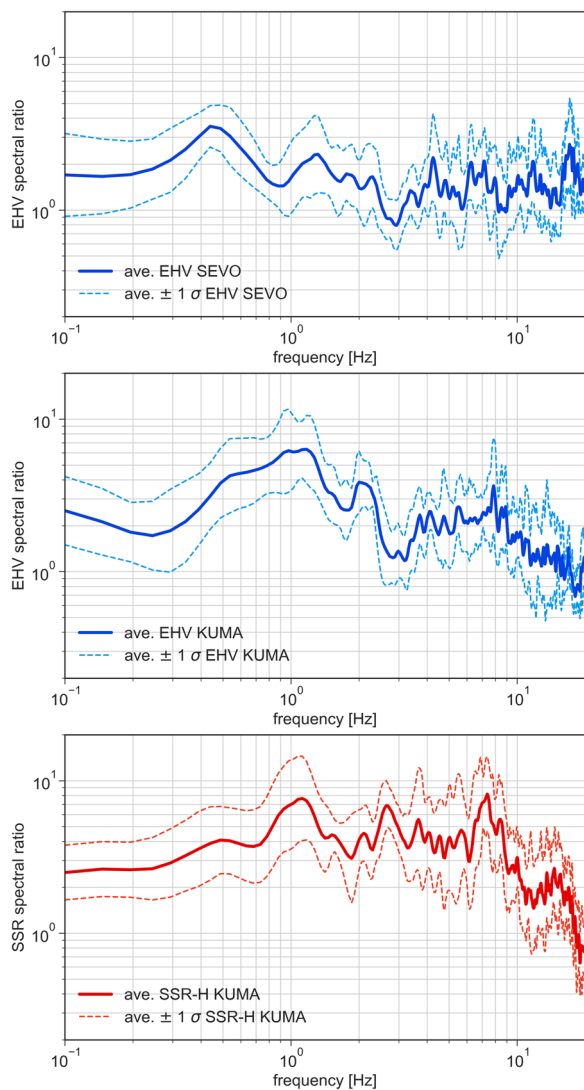
Fig. 3 Empirical amplification functions at KUMA and SEVO sites. Average EHV functions calculated at SEVO reference site (top panel) and KUMA prediction site (middle panel). SSR function calculated at KUMA (bottom panel)

of 120 s, and a logarithmic spectral smoothing algorithm (Konno and Ohmachi 1998) with the default value of 40 for the bandwidth coefficient b. The H/V curves of all the arrays (KUM-SS1, KUM-S, KUM-SM, KUM-M and KUM-LL) consistently show two resonance peaks at about 0.3 and 1.1 Hz with amplitude as large as 4 and 8, respectively (Fig. 4). For the arrays with the largest aperture (KUM-SM, KUM-M and KUM-LL), the second resonance peak slightly increases in frequency up to 1.3 Hz. The systematic lower amplitude of the H/V curve calculated for station 01 is clearly visible from the comparison of the average H/V curves for the 3 lower aperture arrays and is due to the system malfunction of the

NS component. Neglecting this outlier, the average H/V curves are similar and suggest homogenous subsurface conditions for the arrays. As expected, the average curves show larger dispersion (Fig. 4e) for the KUM-LL array, which spans a much wider area in which the homogenous assumption may not strictly hold. However, also for KUM-LL data the two frequency peaks in the H/V ratios are clearly observed. To evaluate the polarization of the estimated frequency peaks, we have also calculated the H/V ratios as a function of rotated horizontal components in the horizontal plane (see Additional file 1). We do not show the results here for the sake of brevity but we did not observe any clear directional dependence of the H/V peaks amplitude along a particular direction, therefore we related the two H/V peaks to the presence of seismic velocity contrasts along the depth profile. Although different peaks in the H/V curves can be also related to the presence of Rayleigh-wave higher modes (Arai and Tokimatsu 2004), given the objective difficulties of proper mode addressing, we based our further analysis on the simplified assumption that the observed H/V peaks are both related to the contribution of the fundamental mode Rayleigh wave.

H/V curve is considered as a proxy for the Rayleigh wave ellipticity (Fäh et al. 2003), but the similarity of actual H/V and ellipticity is controlled by the relative proportion of Rayleigh waves and other seismic phases in the AMV wavefield (Molnar et al. 2022). To extract the Rayleigh wave ellipticity curve to be used in surface wave inversion and evaluate the relative contribution of surface waves and body waves in the H/V composition, the random decrement technique (Raydec; Hobiger et al. 2009) was applied to one station of KUM-S array. This method aims at suppressing the occurrence of seismic phases other than Rayleigh waves by stacking the narrow-band filtered time windows of the signals starting at positive zero-crossing of the vertical component of motion, and projecting the corresponding horizontals into the direction which maximizes the correlation to the vertical with the theoretical 90° phase shift of the Rayleigh wave. Since the method applies to the 3-components of motion, station 1 was discarded due to the malfunction and sensor 7 was selected for the analysis. The Raydec ellipticity curve (Fig. 4f) has a shape similar to the H/V curve calculated for the same station. The two curves have close amplitude above 2 Hz and show a main peak at 1.1 Hz but Raydec ellipticity has a lower amplitude with respect to the corresponding H/V curve (maximum amplitude difference of 2.2 at 1.1 Hz). The Raydec curve stays below the H/V in the frequency range 0.4–2 Hz. The amplitude difference between the curves is almost constant (0.5) in the frequency range 0.4 Hz up to the first trough at 0.6 Hz. Finally, Raydec ellipticity shows a lower frequency

Hailemikael *et al. Earth, Planets and Space*   (2023) 75:105

Page 9 of 25
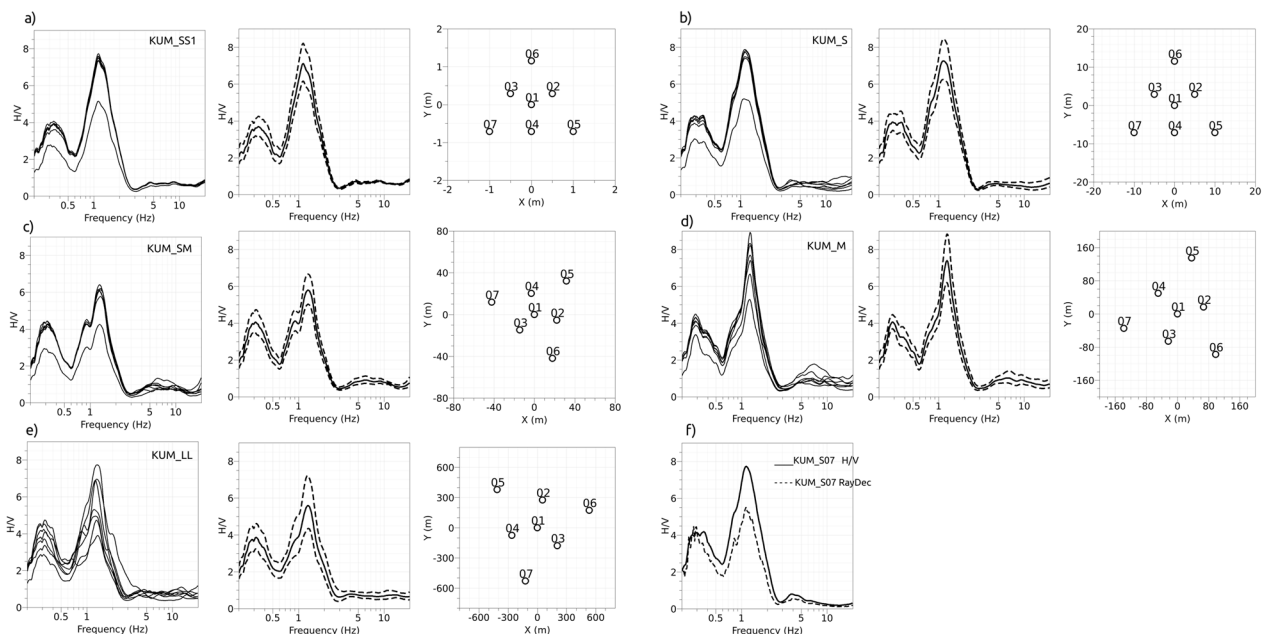
Fig. 4 H/V curves at the five arrays with increasing aperture: KUM_SS1 (**a**), KUM_S (**b**), KUM_SM (**c**), KUM_M (**d**) and KUM_LL (**e**). The average H/V curves at the seven stations (solid curves, in left panels), their mean curve with standard deviation (solid and dashed lines in middle panels), and array geometry (open circles in right panels) are also shown. The comparison between the average H/V curve (solid line) and the average fundamental Rayleigh wave ellipticity curve (dashed line) obtained by Raydec analysis (Hobiger et al. 2009) for station #7 of the KUM_S array is also shown (**f**)

peak than H/V (below 0.3 Hz). This result suggests that whereas a significant uncertainty affects the low frequency resonance, the higher frequency resonance is well retrieved from both methods. In addition, the Rayleigh wave predominance in the ambient vibration wavefield seems confirmed for the higher frequency range (above 2 Hz) where the curves are closer, whereas the relative contribution of the other different phases increases and varies with frequency in the lower range.

Vs-profile retrieval from AMV data

To retrieve the surface-wave DC from AMV data, we employed different techniques and datasets. In particular, the vertical components of AMV recorded at all sensors of the arrays with the largest aperture (KUM-SM, KUM-M and KUM-LL) were analyzed by the cross-correlation (CC) and the Modified Spatial Autocorrelation (MSPAC; Bettig et al. 2001; Wathelet et al. 2005) methods to derive the fundamental-mode Rayleigh-wave DC. 3C AMV data recorded at all sensors composing the largest arrays, excepting for those recorded at the malfunctioning central sensor (station 1) in common with all arrays, were used to retrieve both the fundamental mode Rayleigh- and Love-wave DCs by the high-resolution Rayleigh Beam Forming (RTBF) technique. The CC analysis was implemented by ad hoc software (Vassallo et. al. 2019; Di Giulio et al. 2020) whereas MSPAC and RTBF

analyses were performed by using the Geopsy software suite (Wathelet et al. 2020). In the following, for the sake of brevity and readability, we focused on the comparison of the results from each method and their combination to derive the inversion target DCs rather than on the processing details. Interested readers are referred to the supplementary materials for an exhaustive description of the processing steps adopted in each technique (see Additional file 2).

DC data obtained from the different methods show a very good agreement (Fig. 5), and allow to select a final Rayleigh curve in a wide frequency band (from 0.71 to 20 Hz). DCs and their uncertainties (please see Additional file 2) derived from different methods were combined, i.e., resampled and averaged in the slowness domain, producing a final uncertainty at a given frequency (shown as error bar in Fig. 5).

The Rayleigh-wave DCs obtained by the three methods are within their experimental uncertainty in the frequency range 1.5–8 Hz. The most significant discrepancy in the DCs is observed in the lowest frequencies part (below 1 Hz) where RTBF analysis gives higher phase-velocities with respect to MSPAC analysis (Fig. 5d). We decided to select DC data for the lowest frequencies based on the MSPAC curve, because the spatial autocorrelation method in principle can provide a better resolution (Ohori et al. 2002) assuming the

Hailemikael *et al. Earth, Planets and Space* (2023) 75:105

Page 10 of 25

plane-wave stationarity and an isotropic AMV wavefield. Table 2 summarizes how the target DC was built: the target Rayleigh DC was selected combining the MSPAC results below 1 Hz (using data from KUM_LL to KUM_S arrays), the CC results above 8 Hz and averaging the DCs obtained from the three methods in the range 1.5–8 Hz. Only the RTBF analysis exploited the AMV horizontal data providing the Love-wave DC in the range 0.74–3.5 Hz.

Rayleigh and Love dispersion curves were jointly inverted for deriving an S-wave velocity profile through an improved neighborhood algorithm as developed in Geopsy (Wathelet 2008). Since the results of the geotechnical and geophysical investigation (OYO 2020) were not yet released to the participants of the blind prediction step 1 at the time of the inversion, the model parameter space (Table 3) was mainly based on the information available from the JIVSM and J-SHIS models for Vs and densities and on the Chimoto et al. (2016) model for Vs and densities in the very shallow part of the profile (Fig. 2); in particular, we tested different model parameterization during the inversion and the better fitting results were obtained using seven uniform layers overlying the half-space (Table 3 and Fig. 6). S-wave velocities were allowed to vary in a range of ±50% with respect to the values in the reference models. A linear increase of
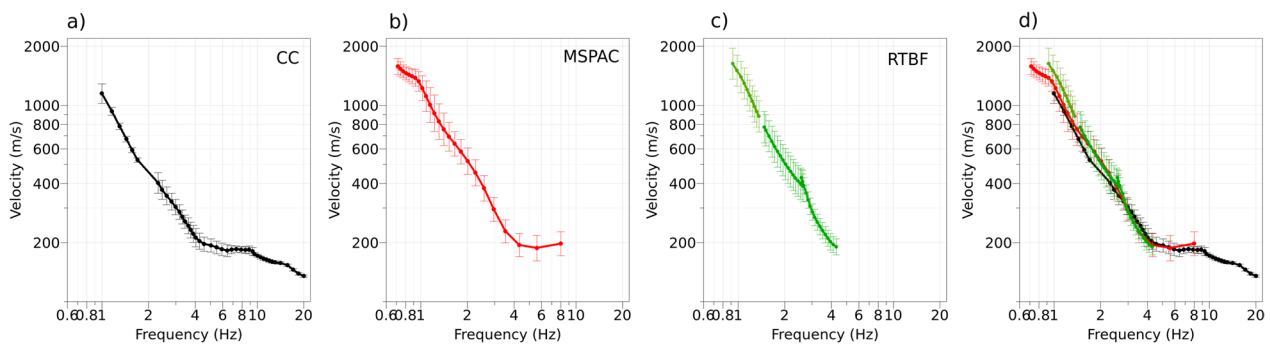
**Fig. 5** Rayleigh-wave DC estimated using Cross-correlation (**a**), MSPAC (**b**) and RTBF analysis (**c**). The DCs are overlaid in **d**

Table 2 Frequency range limits of DCs from array analysis

Array name	CC (used for Rayleigh dc) frequency band (Hz)	MSPAC (used for Rayleigh dc) frequency band (Hz)	RTBF (used for Love dc) frequency band (Hz)
KUM_S	9.6–20	3.5–9.0	
KUM_SM	8–9	2.5–3.2	2.5–3.5
KUM_M		1.8–2.2	1.3–2
KUM_LL		0.7–1.2	0.74–1.1

Table 3 Model parameterization used in the inversion

Layer #	Velocity–depth relation	Vp range [m/s]	Vs range [m/s]	Density [kg/m^3] (fixed)	Poisson ratio	Thickness range [m]
1	Linear increase for Vs uniform for Vp	140–420	from 80–200 to 100–250	1600	0.2–0.5	1–25
2	Uniform	430–1300	250–750	1800	0.2–0.5	1–25
3	Uniform	900–2000	350–750	1950	0.2–0.5	5–215
4	Uniform	1500–2500	800–1200	2070	0.2–0.5	10–400
5	Uniform	1500–3000	650–2000	2200	0.2–0.5	10–200
6	Uniform	1500–4000	1000–3000	2350	0.2–0.5	20–800
7	Uniform	2500–4500	1200–3600	2450	0.2–0.5	50–2000
Half-space		2500–6900	1600–4800	2700		

Hailemikael *et al. Earth, Planets and Space*   (2023) 75:105

Page 11 of 25
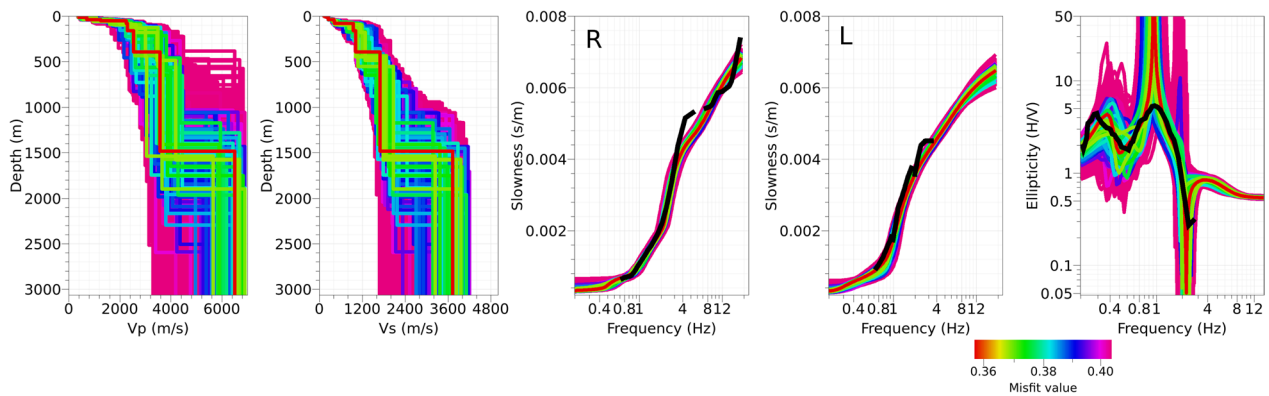
Fig. 6 From left to right: Vp and Vs models derived from the joint inversion of Rayleigh (R), Love (L) DC (fundamental mode), and with the absolute Rayleigh-wave ellipticity. The experimental curves are plotted in black, whereas the models are plotted in a color scale proportional to the misfit obtained during the inversion. The best model (i.e., minimum misfit) is shown in red color

S-wave velocity with depth was allowed for the uppermost layer (maximum thickness of 25 m; see Table 3). Both density and P-wave velocity were linked to Vs profile, Vp with the condition of the Poisson's ratio to be within the range 0.2–0.5.

Although the inversion software allows for taking into account the ellipticity sign (i.e., prograde or retrograde Rayleigh-wave particle motion), we used the absolute value of the fundamental mode Rayleigh-wave ellipticity derived by Raydec analysis (Fig. 4f) as an additional inversion constraint because of its clear depiction of both ellipticity peaks at about 0.3 Hz and 1.1 Hz. In fact, in addition to the Raydec method, the RTBF method allows for the extraction of Rayleigh wave ellipticity as well; to this aim we performed some tests and found that the two methods provide consistent results for frequencies above 0.6 Hz, whereas the Raydec method outperforms RTBF in the low frequency range where the ellipticity peak around 0.3 Hz was observed (please refer to Figure D of Additional file 2).

During the inversion, we fixed an equal weight to all input data (dispersion and ellipticity curves). We tried to fit the two ellipticity peaks at about 0.3 Hz and 1 Hz and the main trough at about 3 Hz of the fundamental mode Rayleigh-wave ellipticity curve. Overall, we obtained a good fit between our results and the observations (Fig. 6). The results are shown for a misfit value lower than 0.4, where misfit is calculated as (Wathelet et al. 2008):

$$misfit = \sqrt{\sum_i \frac{(xd_i - xc_i)^2}{\sigma_i^2 n_f}},$$

with xd_i and xc_i representing the observed and the calculated data sample at frequency i, σ is the data standard deviation and n_f is the number of frequency samples.

The best fit model (misfit = 0.36) shows shallow velocities ranging from 150 to 250 m/s in the top 20 m. Vs increases up to 400 m/s down to 80 m depth, where a first Vs discontinuity is found and the velocity increases at about 1000 m/s. The Vs profile shows this last value down to roughly 400 m depth, where a second Vs sudden increase to 1700 m/s is observed. The main seismic impedance contrast is estimated at a large depth around 1500 m, where the seismic bedrock Vs is estimated to be larger than 3700 m/s. It is worth noting that the bedrock depth estimate is mainly controlled by the low-frequency peak in the ellipticity curve.

1D ground motion simulations

We simulated the weak motions (Mj 5.9, step 2) observed at the prediction site KUMA by the STRATA code, which allows performing 1D total stress ground response analysis in the frequency domain (Kottke and Rathje 2008). This code takes into account nonlinearity of subsurface materials through the equivalent-linear (EQL) approach (Schnabel et al. 1972), an iterative procedure for which the assigned properties of the viscoelastic subsurface layers, namely normalized shear modulus (G/G_0) and material damping ratio (D), are iteratively adjusted to be consistent with the effective level of shear strain (γ %) induced by the input motion. The EQL implementation requires that for each viscoelastic layer of the 1D model the values of thickness, unit weight, shear-wave velocity (Vs) and normalized shear modulus reduction and damping curves as a function of γ are specified. For the shallower layers, nonlinear modulus reduction and damping curves (Table 4) were drawn from laboratory tests (Fig. 7) and from the literature (Rollins et al. 1998), taking into account the information included in the OYO report (OYO 2020), which was made available at this stage of the blind prediction exercise. In particular, this

Hailemikael *et al. Earth, Planets and Space*   (2023) 75:105

Page 12 of 25

Table 4 1D EQL model parameters; the codes T1, T2, T3 and T4 refer to shear modulus reduction and damping curves estimated by laboratory testing (OYO 2020) and shown in Fig. 7

Layer number	Depth (m)	Thickness (m)	Unit weight (kN/m^3)	Vs (m/s)	Modulus reduction and damping curves
1	0.00	2.79	14	143.00	T1 sample
2	2.79	2.79	14	166.00	T1 sample
3	5.58	2.79	13	189.00	T2 sample
4	8.37	2.79	13	213.00	T2 sample
5	11.16	2.79	19	236.00	T3 sample
6	13.95	17.00	18	253.00	T4 sample
7	30.95	6.91	18	253.00	T4 sample
8	37.86	12.87	18	406.00	Rollins et al. 1998
9	50.73	29.29	18	420.00	Rollins et al. 1998
10	80.02	80.81	21	949.00	Linear
11	160.83	231.25	21	1020.00	Linear
12	392.08	1092.94	23	1700.00	Linear
13-Half-space	1485.02	#	27	3728.00	#
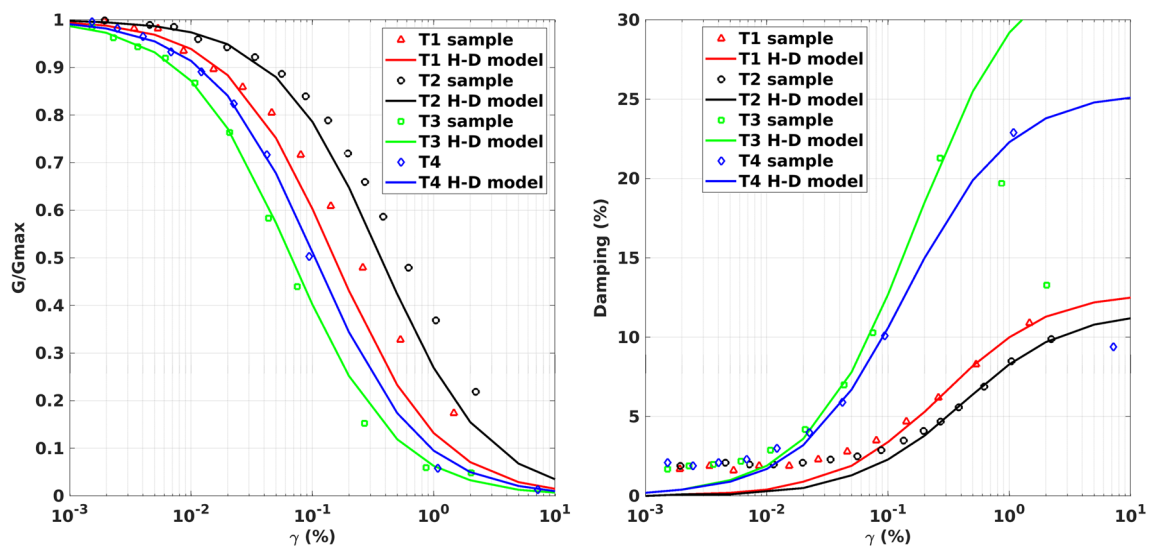
Fig. 7 Nonlinear modulus reduction (G/G$_0$ vs shear strain-γ) and damping (D vs shear strain-γ) curves obtained from cyclic triaxial testing of soil samples collected at the KUMA site. The symbols represent the experimental data while the solid lines represent the Hardin and Drnevich (1972) hyperbolic model fitting of the experimental data (H–D model). T1 sample was collected at depths between 4 and 5 m, T2 between 7.7 and 8.7 m, T3 between 13 and 14 m and T4 between 20 and 21 m (redrawn from OYO, 2020)

report includes both the results of cyclic triaxial laboratory testing performed on the specimens and the hyperbolic model fitting of the G/G0-γ and D-γ curves for each sample as proposed by Hardin and Drnevich (1972). In our modeling, we decided to use the experimental data (colored symbol in Fig. 7) except for the damping estimation at shear strain levels larger than 0.1%, where we used the hyperbolic model.

Although the software allows taking into account for the variability of the input model parameters (thickness, velocity and nonlinear properties) by a Monte Carlo approach, which generates a distribution of output, we decided to proceed in the simulation without including model parameter variations to simplify the comparison between ground motion predictions and observations, particularly in terms acceleration time series. We leveraged the code automatic sub-layer discretization to allow

for seismic energy transmission at frequencies up to 25 Hz, and maximum iteration number was set equal to 20.

In addition to EQL 1D simulations by STRATA, we also performed a 1D total stress ground response analysis by the Deepsoil software (Hashash et al. 2020) to predict horizontal strong ground motions (Mj 6.5, step 3). This code allows performing fully nonlinear (NL) ground response analysis in the time-domain by integrating the equation of motion in small time steps. This approach fully accounts for nonlinear behavior of subsurface materials through cyclic nonlinear stress–strain models. As a constitutive model for the shallower layers (Table 5), we used an extended version of the modified Kondner–Zelasko constitutive model (MKZ) developed by Matasović and Vucetic (1993). The modulus reduction and damping pressure-dependent hyperbolic model fitting procedure (MRDF; Hashash et al.2020) was used to fit nonlinear normalized shear modulus reduction and damping curves associated with each model layer. This procedure includes a frequency-independent damping as proposed by Phillips and Hashash (2009). In this case, we divided each layer model into sub-layers with thickness h_s to allow for seismic energy transmission up to the maximum frequency f_{max}= 30 Hz by the following formula:

$$h_s = Vs/4f_{max},$$

where *Vs* is the layer shear-wave velocity.

For both EQL and NL 1D simulations, input accelerations were the horizontal ground motion (NS and EW components) recordings acquired at the reference site SEVO for the Mj 5.9 and Mj 6.5 earthquakes. These signals were baseline corrected (processed by de-trending, zero padding and high-pass filtering with 0.1 Hz corner frequency), converted to acceleration time-histories and applied at the half-space level implementing an elastic base boundary condition, therefore considering the input as outcropping motions. The adopted Vs model was that obtained from AMV data analysis as described in subsection "Vs-profile retrieval from AMV data" Section.

For the nonlinear model of the Mj 6.5 foreshock (step 3), the Vs subsurface model was adapted to the layer discretization needed to correctly perform the nonlinear analysis, namely by fulfilling the following condition: sub-layer thickness $h < = Vs/(4 \,{}^*f_{max})$, where f_{max} is the maximum frequency of analysis which was set equal to 30 Hz. The 1D nonlinear model is summarized in Table 5, including layer discretization (n# of sub-layers and thickness of each sub-layer). Model was built similarly to what was described for the EQL case. Table 5 also includes target modulus reduction and damping curves for the fitting of the MRDF pressure-dependent hyperbolic model. Similarly to the EQL case, we assumed linear viscoelastic stress–strain behavior with constant damping ratio of 1% for the deeper layers (i.e., at depth larger than about 80 m).

Results

Shear-wave velocity structure at the prediction site

AMV data collected at the KUMA prediction site are characterized by a significant contribution of surface waves, and the use of arrays with increasing aperture allowed to derive surface-waves dispersion curve data in a wide frequency range (from 0.7 to 20 Hz). Moreover the geometry composed of two nested triangles using seven seismic stations proved very convenient since it allowed for good azimuthal coverage of surface-wave propagation fronts with a limited number of stations. We have

Table 5 1D NL model parameters

Layer	n# of sub-layers	Sub-layer thickness (m)	Sub-layer unit weight (KN/m^3)	Vs (m/s)	Constitutive model
1	3	1	14	143.00	MKZ
2	3	1	14	166.00	MKZ
3	3	1	13	189.00	MKZ
4	3	1	13	213.00	MKZ
5	3	1	19	236.00	MKZ
6	8	2	18	253.00	MKZ
7	3	2	18	253.00	MKZ
8	4	3	18	406.00	MKZ
9	9	3.5	18	420.00	MKZ
10	10	8	21	949.00	Linear
11	27	8.5	21	1020.00	Linear
12	77	14	23	1700.00	Linear
13-Half-space	#	#	27	3728.00	#

adopted different techniques of analysis obtaining very consistent results in terms of fundamental mode Rayleigh-wave dispersion data (Fig. 5d). Further, the Raydec and RTBF analyses allowed to extract Rayleigh-wave ellipticity and the fundamental mode Love-wave dispersion curves, respectively.

The best fit model derived from the joint inversion of DC and ellipticity data shows a good agreement between experimental and theoretical curves, except in the frequency band 4–6 Hz where the theoretical Rayleigh DC is not able to follow the inflection of the experimental DC (Fig. 6). The ESG6 Committee has provided its "consensus" model for the target site based on literature data. We compared this "consensus" model with our results in Fig. 8, finding a satisfactory agreement between the two models.

It is worth mentioning that even if we adopted the simplified assumption of both ellipticity peaks related to the Rayleigh wave fundamental mode, the fair agreement in the Vs structure obtained by our joint inversion of DC and ellipticity data and that provided by the ESG6 committee, suggests that this assumption may hold true in our case.

The first 400 m of the Vp and Vs profiles are very similar, and also the deep seismic contrast around a depth of 1500 m is found in both models. The main difference between the two is in the depth of the intermediate seismic velocity contrast, which is found at a depth of about 400 m in our model versus 600 m in the "consensus" model. On average, our model shows lower Vs values than the "consensus" one between 400 and 1500 m, and some large discrepancies are also observed in the density values. The density was fixed during our inversion (Table 3) because of its low influence on dispersion curves, and we did not consider the "consensus" density profile that was released by ESG6 committee only after the inversion blind exercise (at the end of step1).

The comparison between the two models is also performed in terms of SH transfer functions (Fig. 8) computed by the reflectivity method (Kennett and Kerry 1979). Both functions point out that the main ground motion amplification should be observed in the 1–2 Hz frequency range, with SH transfer functions showing some differences in the amplification level, mainly in the lower frequency range (i.e., < 1 Hz) and between 1.5 and 2 Hz.

1D simulation results

The 1D simulations predicted significant horizontal ground motion amplification at the KUMA site with respect to SEVO, where the seismic input was recorded, for both weak- and strong-motion input. For the M 5.9 earthquake (step2), the predicted time series by the EQL approach shows PGA of about 0.036 g for the EW component and of about 0.049 g for the NS component (Table 6 and Fig. 9c, d). Such prediction is in very good agreement with the observation for the EW ground motion recorded at the KUMA site (0.034 g; Fig. 9a, c), whereas peak ground motion for the NS component is largely overestimated by 45% (Fig. 9b, d).

The comparison of Fourier amplitude spectra (FAS) shows that the 1D EQL predictions have larger amplitude

Table 6 Values of peak ground acceleration (PGA) from observations at KUMA (obs), Strata EQL model (strata) and fully nonlinear model (deepsoil)

	PGA EW component (g)	PGA NS component (g)
Mj 5.9	0.034 (obs)	0.031 (obs)
	0.036 (strata)	0.049 (strata)
Mj 6.5	0.396 (obs)	0.45 (obs)
	0.315 (strata)	0.317 (strata)
	0.183 (deepsoil)	0.145 (deepsoil)
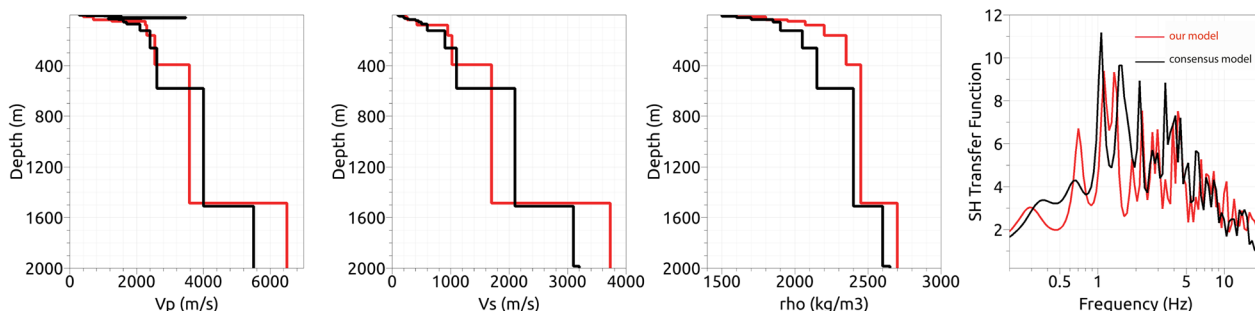
Fig. 8 Comparison between our best model (in red) derived from the joint inversion and the "consensus" ESG6 model (in black). The comparison is shown in terms of Vp, Vs, density and SH transfer functions computed by the reflectivity method (Kennett and Kerry, 1979) implemented in the Geopsy software suite (Wathelet et al. 2020). In the SH modeling, P-wave and S-wave quality factors Qp and Qs were set equal to 1/10 of Vp and Vs values, respectively
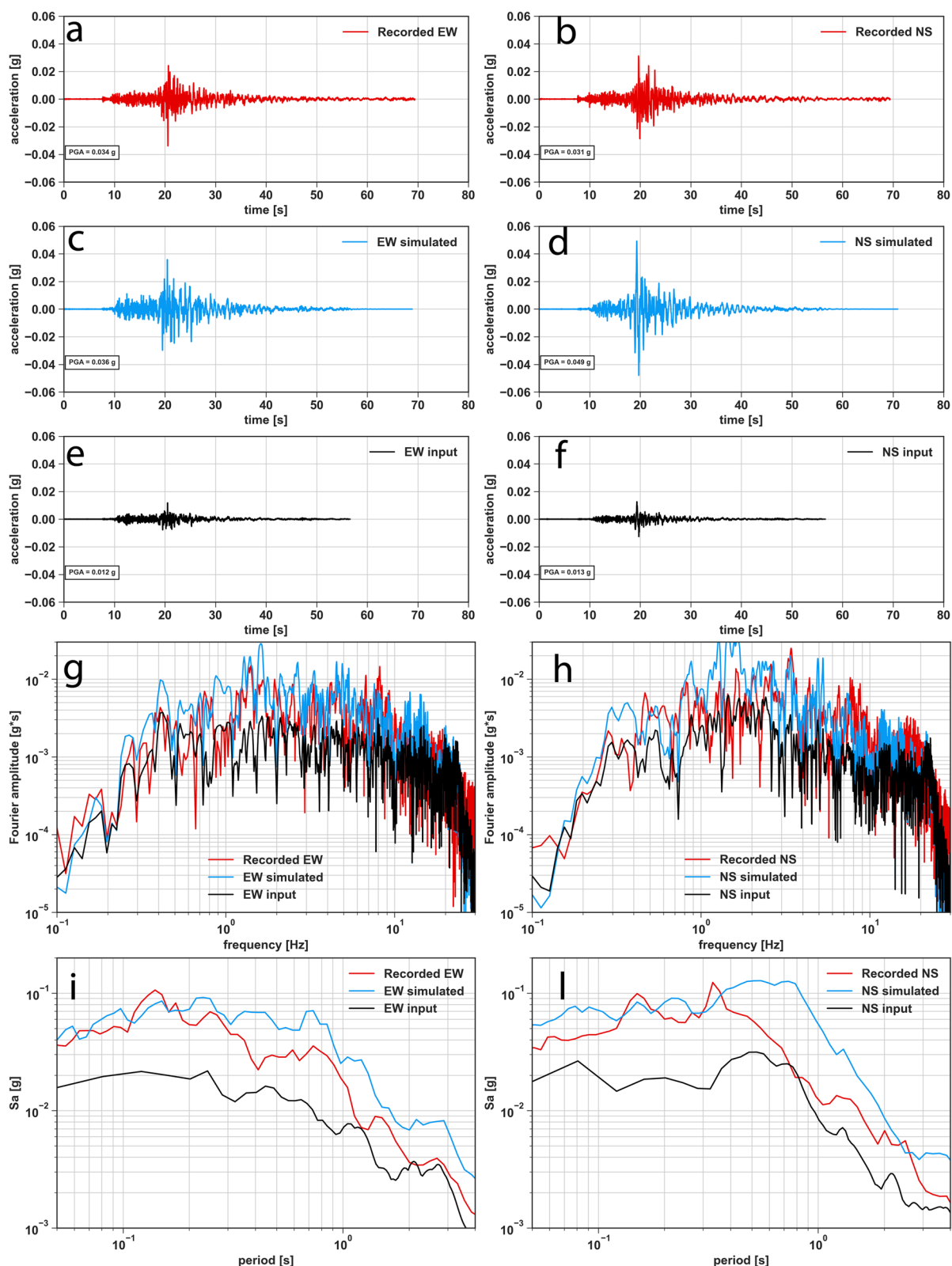
Fig. 9 Mj 5.9 ground motion observations versus 1D EQL predictions for EW and NS ground-motion components (left and right panel, respectively). **a**, **b**, **c**, **d**, **e**, **f** Acceleration time series, for observations (red), 1D EQL predictions at KUMA (blue) and input ground motion recorded at SEVO reference site (black). **g**, **h** Fourier amplitude spectra for input ground motion (black), observations (red) and predictions at KUMA (blue). **i**, **l** 5%-damped acceleration response spectra for input ground motion (black), observations (red) and 1D EQL predictions at KUMA (blue)

Hailemikael *et al. Earth, Planets and Space* (2023) 75:105

Page 16 of 25

than the observations for low frequencies (below 1 Hz), whereas FAS is rather well predicted for the EW component of motion in the range 1–3 Hz (Fig. 9g, h). This is particularly evident from the examination of the FAS calculated for the NS component of the ground motion in the frequency band 1–2 Hz (Fig. 9h). It is worth noting that in this frequency band, the NS input ground motion component has FAS 3 times larger than the EW input component, so large that the NS input FAS is comparable to that observed at KUMA (Fig. 9h), thus explaining the differential response predicted at the surface due to the two input motions.

This frequency- (or period T)dependent ground motion overestimation of the recordings by the 1D EQL predictions is pointed out by the comparison between observed and predicted 5% damped elastic acceleration response spectra (Fig. 9i, l). At KUMA, peaks of the recorded acceleration spectral ordinates (Sa) are observed in the period band between 0.1 and 0.4 s; the larger amplitudes were recorded for the NS ground motion component, with values around 0.13 g (Fig. 9l). In terms of Sa, the predictions largely overestimate the observed EW response spectra for periods above 0.3 s, where the 1D EQL simulations show amplitudes up to 2.3 times larger than the observations (about 0.07 g, Fig. 9i) and the observed NS response spectra in the period band 0.4–2 s, where the predictions are up to 5 times larger than the observations (about 0.125 g, Fig. 9l).

To obtain a more quantitative evaluation of the goodness-of-fit (GoF) between predicted and recorded motions, we used the categories proposed by Kristeková et al. (2009), which are based on time–frequency (TF) representation of the waveforms to be compared and related misfit metrics. In particular, two indices are used to quantify the agreement between signals based on their envelope quantitative comparison (EG), and the phase GoF (PG). In more detail, for two signals where one is the reference, it is possible to calculate the envelope and phase differences between the TF representations of the two signals normalized by the maximum TF of the reference; then, the obtained misfits are transformed such as to assume values in a finite range which allows for the quantitative evaluation of the agreement between the two signals (Kristeková et al. 2009). Therefore, EG can be interpreted as a single integral value of the overall GoF between the envelopes of the analyzed signals and analogously PG for the phase GoF (Kristeková et al. 2006); these finite values of envelope GoF can also be represented as a function of time (TEG) and frequency (FEG) and similarly for the phase GoF as a function of time (TPG) and frequency (FPG). According to the original formulation of Kristeková et al. (2009), EG and PG, along with the other above described GoF parameters,

are allowed to vary in the range 0–10, where 10 means perfect agreement between observed and predicted ground-motion, values below 4 indicate a poor fit, values in the range 4–6 stand for a fair fit, values between 6 and 8 represent a good fit and over 8 are for an excellent fit.

To calculate the GoF, the predicted and recorded ground-motions were bandpass filtered between 0.1 and 20 Hz using a fourth-order non-causal Butterworth filter before computation of their continuous wavelet transform (Daubechies 1992), and the calculation of GoF metrics was obtained through the obspy python package (Beyreuther et al. 2010).

For the Mj 5.9 predictions, the EG values are about 3.5 and 2.5 for the EW and NS horizontal components (Fig. 10), indicating a rather poor amplitude GoF with the observations, whereas the phase GoF is fair for the EW component (PG of about 4.8) and the NS component (PG of about 4). EG as a function of frequency (FEG, insets in Fig. 10) shows that the envelope disagreement between the signals is mainly between 1–2 Hz while PG as a function of frequency (FPG, insets in Fig. 10) shows that the phase disagreement is distributed on a wider frequency band, especially for the NS component.

For the Mj 6.5 Kumamoto foreshock, we compared horizontal strong ground motion predictions obtained using the EQL and NL approaches with the observations. The observed peak acceleration value is about 0.40 and 0.45 g for the EW and NS components (Table 6 and Fig. 11a, b). The input ground motions recorded at SEVO show similar waveforms and PGA values, about 0.12 g for the EW component and 0.10 for the NS (Fig. 11g, h). The output PGA for the EQL simulations is about 0.32 g for both horizontal components (Fig. 11c, d), whereas the PGA is about 0.18 g for the EW component and 0.15 g for the NS component in the case of the NL predictions (Table 6 and Fig. 11e, f). The visual inspection of acceleration time series reveals a fairly good strong seismic phases alignment between predictions and observations; however, the same inspection highlights the strong low-pass filtering effect of 1D site modeling, particularly for the EQL ground-motion predictions (Fig. 11c, d). In fact, the comparison between FAS obtained by EQL and NL predictions and FAS observations at KUMA show that both 1D modeling approaches underpredict the recorded motions (Fig. 11i, l). The underprediction is larger for the NS than the EW component and for frequencies higher than about 5 Hz.

In terms of Sa, the recorded EW 5%-damped elastic response spectra show three main maxima: around 0.15 s, with amplitude of about 0.9 g, around 0.4 s, with amplitude of about 0.7 g and a broad peak centered around 1.0 s, with amplitude of about 0.75 g (Fig. 11m). For this component, the EQL prediction shows a fairly

Hailemikael *et al. Earth, Planets and Space* (2023) 75:105

Page 17 of 25
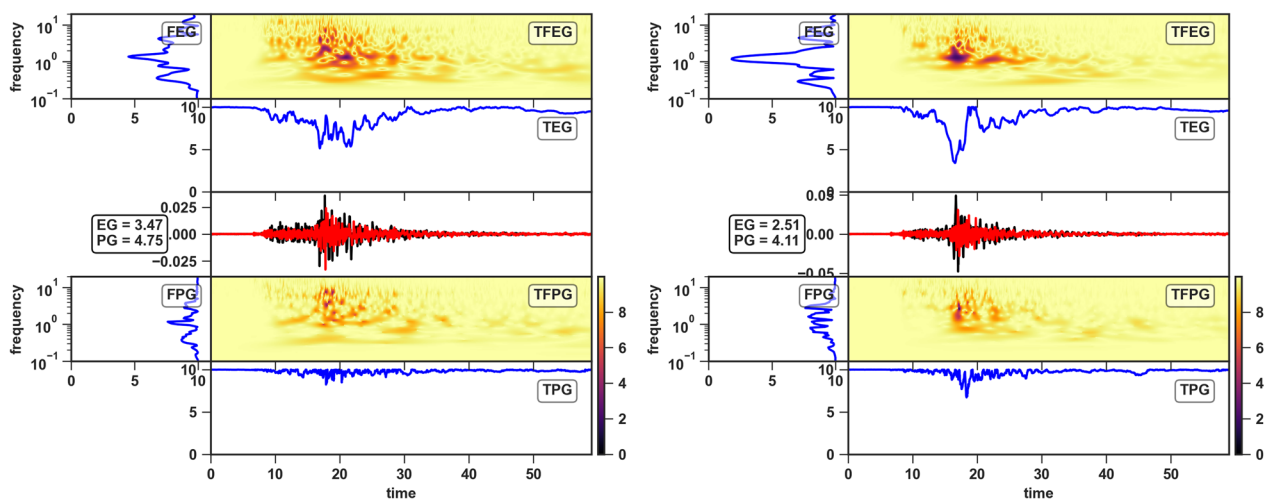
Fig. 10 Comparison between 1D EQL predictions and recorded ground motions at KUMA for the Mj 5.9 earthquake and GoF evaluation following Kristeková et al. (2009). TF representation of the envelope (TFEG) agreement between 1D EQL predictions and recorded ground motions with the evaluation of envelope GoF along time (TEG) and frequency (FEG) axes (upper panels). TF representation of the phase (TFPG) agreement between 1D EQL predictions and recorded ground motions with the evaluation of phase GoF along time (TPG) and frequency (FPG) axes (lower panels). Overall integral GoF metrics for the envelope (EG) and phase (PG) agreement are reported in the black box with values in the range 0–10, where 10 means perfect agreement. Left panels show TFEG and TFPG for the EW component of predicted (black line in middle panel) and recorded (red line in middle panel) ground motions; right panels show the same quantities for the NS components

good agreement for the periods higher than 0.8 s. In fact, the 1D EQL simulated response spectra shows a similar broad peak centered around 1 s with amplitude which is only slightly underestimated (of about 7%) with respect to the observed. The main disagreement of Sa value is in the lower periods (T < 0.8 s), for which the observed Sa is up to 125% larger than the prediction (Fig. 11m). The NL simulation for the EW ground motion component severely underpredicts the observed response spectra in the period range 0.1–2.5 s, with amplitudes lower than 110% at 1.0 s and 125% at 0.15 s (Fig. 11m). Similar considerations hold for the predicted NS elastic response spectra; the shape of predicted and observed response spectra are similar but both EQL and NL predictions systematically underpredict the observed Sa in all periods bands, with larger discrepancies for the NL prediction (Sa amplitudes 2.5 times lower than observations at 0.8 s) (Fig. 11n). As a general consideration, the EQL predictions in terms of maximum Sa are 75% larger than the NL ones and thus show lower disagreement with the observed data (Fig. 11m, n).

We have calculated envelope (EG) and phase (PG) GoF between predicted and recorded horizontal motions also for the Mj 6.5 earthquake (Fig. 12) through the time–frequency misfit analysis of Kristeková et al. (2009). For this earthquake, we obtained larger GoF parameters with respect to the Mj 5.9 event. Amplitude GoF between predictions and recorded ground motion is fair (Fig. 12), with higher EG values (EG of about 5.9 for the EW and 5.7 for the NS components) for the 1D EQL motions with respect to the 1D NL (EG lower than 5.5). Phase GoF is good for both EQL and NL models; the higher values of PG are obtained for the NS component predictions (PG of about 6.8 and 6.7 for the EQL and NL simulations) with respect to the EW (PG of about 6.0 and 6.4 for the EQL and NL simulations).

For the Kumamoto foreshock, we also calculated the maximum shear strain (γ_{max}) vertical profile obtained by EQL and NL simulations; for both approaches, the peak strain is reached at the same depth around 37 m, where the implemented Vs model jumps from about 250 m/s–400 m/s (corresponding to the bottom part of layer #7 in Tables 4 and 5). The differences in terms of strain profile between the two approaches are shown in Fig. 13; for the EW component, the peak shear-strain calculated with the EQL approach (about 0.2%) is about double that of the

(See figure on next page.)
Fig. 11 Mj 6.5 ground motion observations versus 1D EQL and NL predictions for EW and NS components (left and right panel, respectively). **a**, **b**, **c**, **d**, **e**, **f**, **g**, **h** Acceleration time series for EW and NS components. Red, blue, green and black colors refer to observations, EQL and NL ground motions at KUMA, input ground motion recorded at SEVO reference site, respectively. **i**, **l** FAS for input motion (black), observations (red), EQL (blue) and NL predictions at KUMA (green). **m**, **n** 5%-damped acceleration response spectra for input motion (black), observations (red), 1D EQL (blue) and NL predictions at KUMA (green)
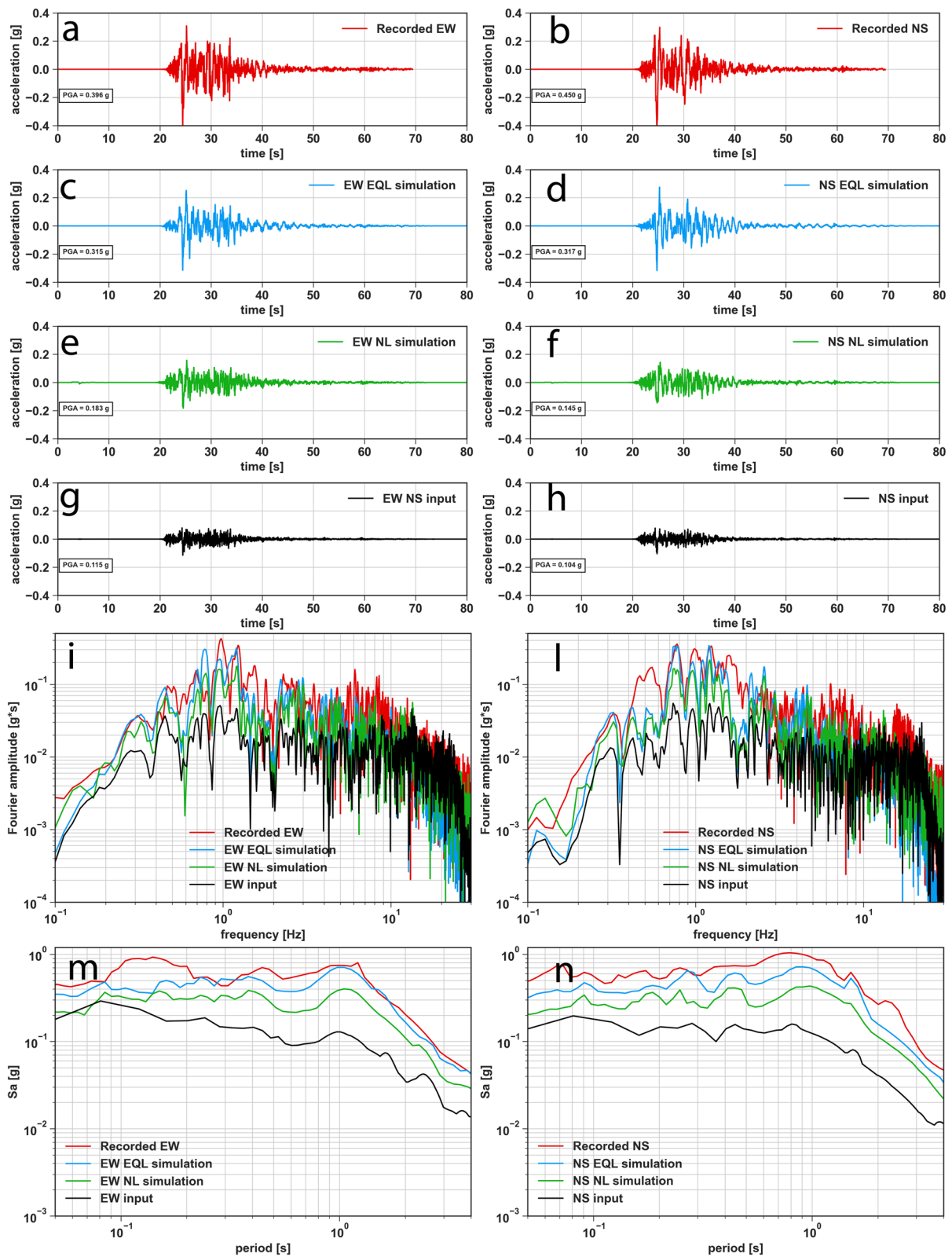
Fig. 11 (See legend on previous page.)
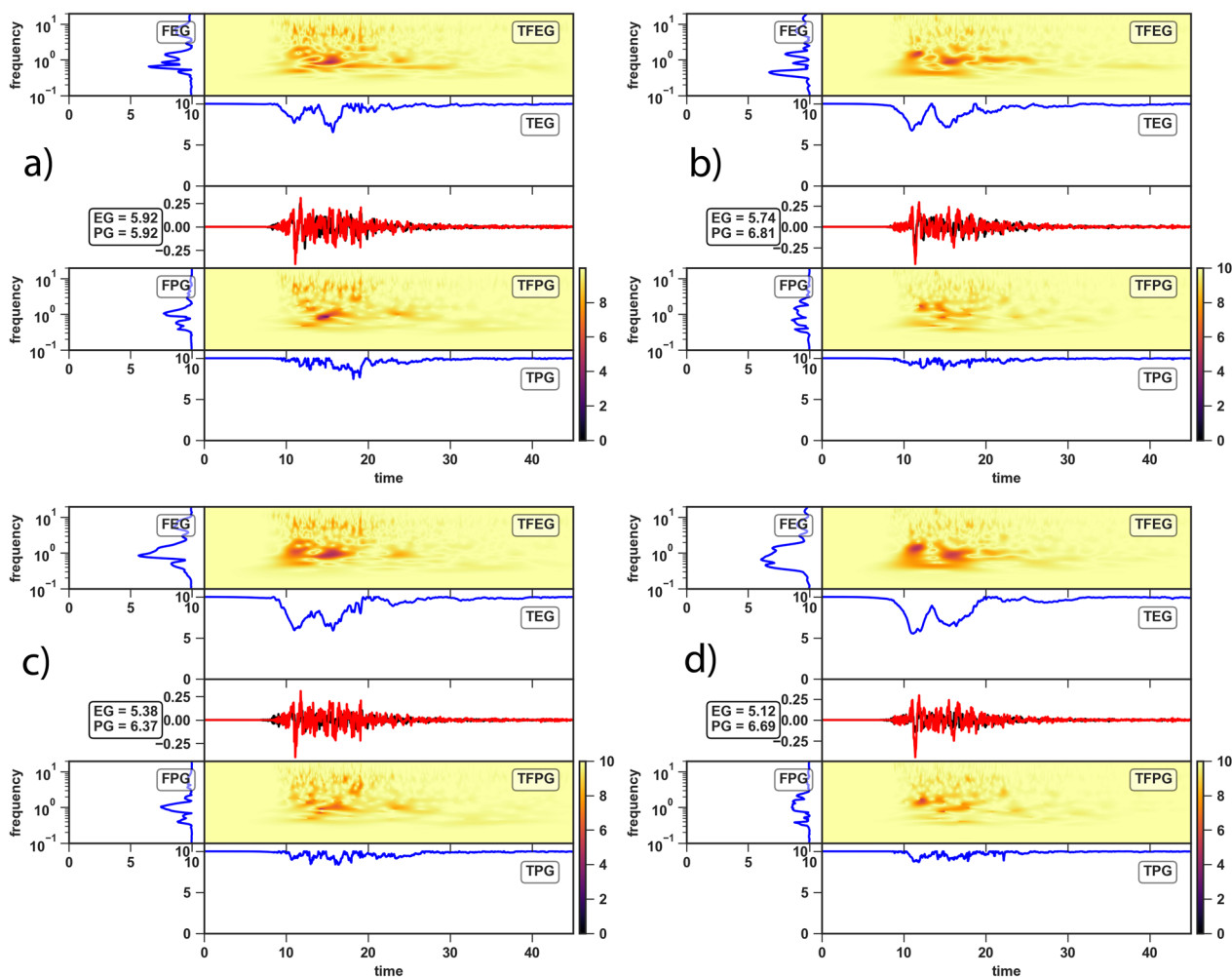
Fig. 12 Comparison between 1D predictions and recorded ground motions at KUMA for the Mj 6.5 earthquake and GoF evaluation following Kristeková et al. (2009). TF representation of the envelope (TFEG) agreement between 1D EQL predictions and recorded ground motions with the evaluation of envelope GoF along time (TEG) and frequency (FEG) axes (**a** and **b** upper panels). TF representation of the phase (TFPG) agreement between 1D EQL predictions and recorded ground motions with the evaluation of phase GoF along time (TPG) and frequency (FPG) axes (**a** and **b** lower panels). Overall integral GoF metrics for the envelope (EG) and phase (PG) agreement are reported in the black box with values in the range 0–10, where 10 means perfect agreement. Left panels show TFEG and TFPG for the EW component of predicted (black line in middle panel) and recorded (red line in middle panel) ground motions; right panels show the same quantities for the NS components. **c** and **d** Show the same quantities and information as in **a** and **b** but for the 1D NL approach

NL one (Fig. 13 left panel). For the NS component the differences are lower, the peak strain is about 0.16% for the NL case whereas it is 0.22% for the EQL case.

In terms of site transfer function, it is remarkable to note that there is a substantial agreement between the estimates of the main site amplification frequency, around 1.2 Hz, obtained by empirical methods, namely the SSR and EHV, applied to weak ground motions (Mj < 5) and the theoretical site transfer function (TTF), which is calculated as spectral ratio between FAS input ground motion and FAS surface EQL prediction at KUMA (Fig. 14). In particular, the denominator of the

TTF is also calculated using weak input motions recorded at SEVO for earthquakes with Mj < 5 (Table 1); for such input motions the calculated TTFs overlap and the soil nonlinear behavior is negligible (the maximum shear strain is equal to 0.015% in our EQL prediction and is reached for the NS component at a depth of about 37 m). The agreement between all three curves is satisfactory in the range 1–2 Hz. Beyond this frequency, the EHV shows lower amplitudes with respect to the SSR, which is considered a more robust estimator of the site amplification function. The agreement between TTF and the average SSR extends to higher frequency up to 4 Hz, where the
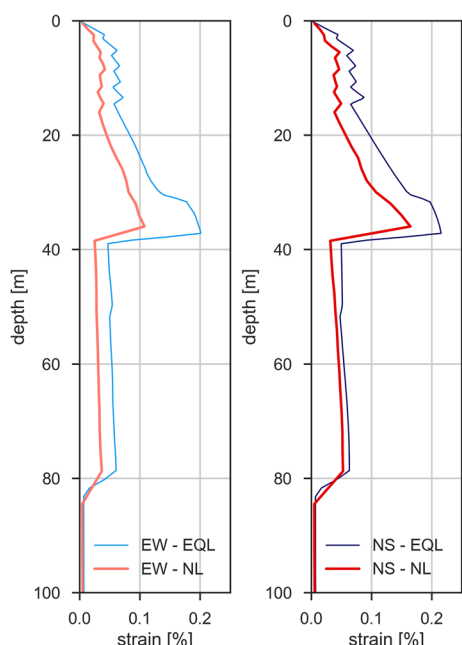
Fig. 13 1D EQL and NL peak shear strain profile predictions for the Mj 6.5 Kumamoto earthquake considering the EW ground motion component (left panel) and NS component (right panel) of the input motions
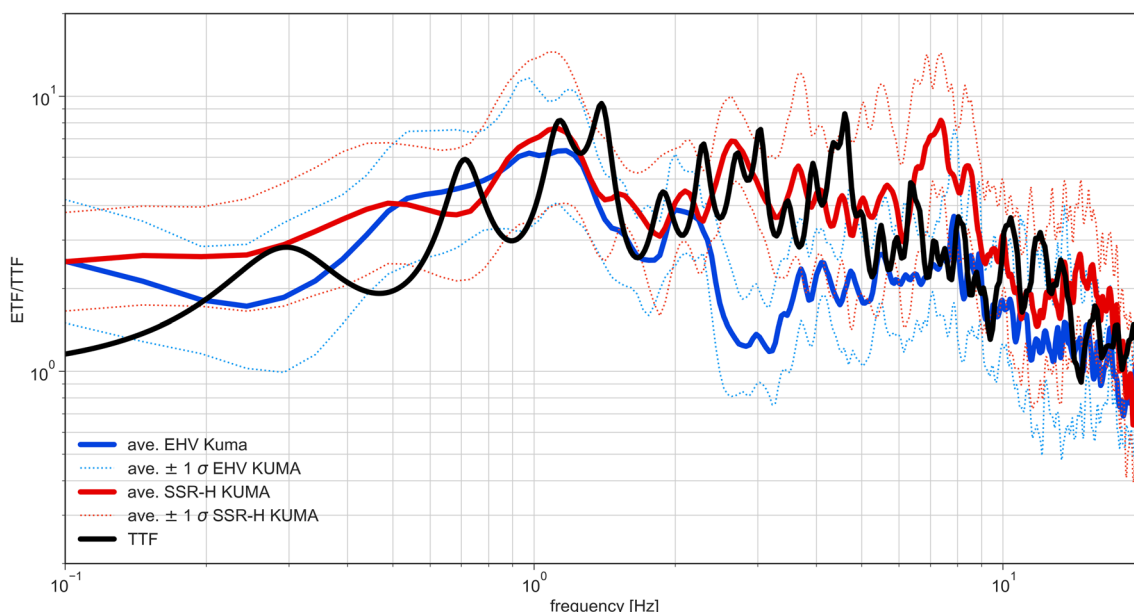
both EHV and TTF up to 9 Hz (Fig. 14). Above 10 Hz, the average empirical transfer functions and TTF fall within the average ± 1σ bounds of the expected value and reduce with increasing frequency. It is worth noting that the empirical amplification functions did not pointed out any clear low frequency peak around 0.3 Hz as shown in the H/V curve based on AMV data, likely because of the different sensitivity of the instrumentation used to record earthquake signals at the KUMA site (accelerometer) and AMV (short period sensors) and likely due to the short time-windows used to analyze the earthquake data.

Discussion and conclusions

We analyzed AMV data collected in the Kumamoto alluvial plain (Chimoto et al. 2023) to retrieve a large depth Vs model for the KUMA site and used this model, in combination with available geotechnical information for the site (Matsushima et al., submitted to Earth Planets and Space), to evaluate the agreement between horizontal ground-motion predictions obtained for the Mj 5.9 aftershock (Step 2) and for the Mj 6.5 foreshock (Step 3) of the Kumamoto sequence and the recorded ground-motions at KUMA (Tsuno et al., submitted to Earth Planets and Space). We calculated predicted weak- and strong-ground motions by 1D GRA implementing an EQL model for the Mj 5.9 earthquake and both EQL and NL models for the Mj 6.5 earthquake.

The comparison between Vs structure obtained by AMV-based site characterization methods and by

TTF remains within the uncertainty range of the SSR curve. At higher frequencies, the SSR shows substantially higher amplitudes (up to 2.5 times larger at 7.5 Hz) than

Fig. 14 Comparison between empirical transfer functions calculated at KUMA (red and blue curves with their relative uncertainties) and theoretical transfer function calculated by 1D EQL modeling for the same site (black curve). Empirical transfer functions were calculated for the events in Table 1 with Mj < 5.9

independent information proved the reliability of passive surface-wave testing to derive large depth Vs estimation. The adoption of different techniques of analysis (MSPAC, CC, and RTBF) allowed us to verify the consistency of DC data estimation between methods and to derive a fundamental mode Rayleigh-wave dispersion curve in a large frequency band (Fig. 5). The dispersion curve is very consistent with the one produced by other teams involved in the blind exercise (Chimoto et al. 2023), confirming that the estimation of the surface-wave dispersion curve can be easily computed from the codes nowadays available in the research community. The extraction of Rayleigh-wave ellipticity (Hobiger et al. 2009), as well the estimation of a Love-wave dispersion curve using a three-component array data analysis (Fäh et al. 2008), provided additional constraints to proceed with a joint inversion. We are satisfied with the Vs profile extracted from the joint surface-wave inversion; our group of best Vs fitting models (Fig. 6) for the Kumamoto target site is in reasonably good agreement with the "consensus" Vs profile distributed by the ESG6 committee (Fig. 8). Particularly interesting is that the joint inversion of Rayleigh-, Love-waves DC and Rayleigh-wave ellipticity curve, which is characterized by two clear frequency peaks (centered around 0.3 and 1.1 Hz), provided useful information to constrain the presence of the significant seismic impedance contrasts, including the deep interface at about 1.5 km (Fig. 8). Such convenient integration of AMV-based advanced analysis techniques provided being very effective (Hobiger et al. 2021) and we believe that should be more frequently adopted in the engineering practice, however this would still need additional initiatives for the transfer of knowledge between the research community and practitioners (Bard et al. 2010; Garofalo et al. 2016a, 2016b).

Despite the retrieval of large depth velocity information and the availability of detailed geotechnical information at the site, rather difficult to have in the current state-of-practice, our simulations of the recorded motions (Tsuno et al., submitted to Earth Planets and Space) provided results which are rather controversial regarding the prediction capability of simplified 1D EQL and NL GRA for both events.

For the Mj 5.9 event, we obtained a reasonable agreement between 1D EQL and recorded ground motions in terms of PGA, in particular for the EW component (Fig. 9 and Table 6). A more in-depth analysis of the GoF by quantitative TF misfit criteria (Kristeková et al.2009) reveals a poor to fair agreement in terms of amplitude envelopes, and a fair agreement in terms of phase alignment (Fig. 10). In particular, for the predicted NS component of ground motion, excessive harmonic components around 1.2 Hz in a short time-window around the strong

phase arrivals are produced by 1D EQL simulations with respect to the recorded motion (Fig. 10, right-top panel).

In terms of Sa (Fig. 9i, l), we observed a large overestimation of both observed horizontal motions, on average around 70% for the EW and 95% for the NS component, with larger residuals at intermediate periods (0.5 s < T < 1.0 s), this is likely due to the frequency dependent amplification of the site, which has estimated fundamental resonance frequency in the range 1–2 Hz (Fig. 14). Such result is in disagreement with the findings of Kaklamanos and Bradley (2018), who compared a large dataset of recorded ground motions at the KiK-net vertical array sites and simulated ground motions by 1D GRA. In general, these authors found that 1D GRA produces ground motions which underpredict short periods parameters (Sa (T < 0.5 s)) and that this underprediction is dependent on the predicted maximum shear-strain (γ_{max}): the lower is γ_{max}, the larger is the underprediction. In our case, for the Mj 5.9 weak-motion where lower γ_{max} values are expected with respect to the Mj 6.5 event, we observe that the short periods parameters are overpredicted instead of underpredicted, in particular for the NS ground-motion component.

Response spectral ordinates underprediction was calculated by 1D EQL and NL models of the Mj 6.5 Kumamoto earthquake (Fig. 11). The average underprediction is of about 20% for the EW component and 34% for the NS component of the EQL model, and of about 47% for the EW component and of 66% for the NS component of the NL model. Larger biases are observed in the range 0.5–0.7 s and around 2.2 s for the NS component of the NL model. For the EW component, the EQL model still shows an acceptable agreement with observations (Fig. 11), although with an underprediction mostly for intermediate periods in the range 0.8–1.2 s (Fig. 11, left panel), while for the NS component, the systematic bias extends to higher periods (Fig. 11, right panel).

The TF measure of the GoF between predicted and recorded ground motions for the Mj 6.5 event shows fair agreement in terms of amplitude and good agreement in terms of phase, for both 1D EQL and NL models (Fig. 12). Focusing on the envelope disagreement, both 1D EQL and NL predictions lack low-frequency components, below 2 Hz, in a 10- to 15-s-long time-window starting from the strong phase arrivals with respect to both horizontal component recordings.

We speculate that the long period energy in the recorded signal could be related with the properties of the available input motion or with propagation of basin-edge generated surface waves from the alluvial plain margin to the N (Fig. 1). While the latter hypothesis should be tested against more advanced 2D (Bordoni et al 2023) and 3D modeling of the source and seismic wave propagation

Hailemikael *et al. Earth, Planets and Space*   (2023) 75:105

Page 22 of 25

in the Kumamoto basin, we argue that the selection of the input motion is a critical choice. In particular, the EHV function at the reference SEVO site (Fig. 3) suggests that this site could be affected by intermediate (between 1 and 2 Hz) and low frequency (below 0.6 Hz) site amplification. Therefore, when using the recorded motion at SEVO as input for 1D ground motion prediction, we may introduce in the 1D simulations more low and intermediate frequency energy than really occurred. Thus, this may cause an overprediction of the observations for the more distant and lower magnitude earthquake (Mj 5.9), and an underprediction for the larger magnitude earthquake (Mj 6.5) due to larger strains induced in the 1D soil column model by the excess of energy. The hypothesis of frequency dependent amplification at SEVO could also explain the different bias obtained by the 1D EQL and NL simulations for the Mj 6.5 event, given that predictions in terms of response spectral ordinates obtained by the two approaches start to deviate for peak shear strains (γ_{max}) similar to those estimated by our simulations (Fig. 13), that is for γ max in the range 0.1–0.4% as a function of period (Kaklamanos and Bradley 2018); however this hypothesis should be investigated by performing additional 1D simulations using different input motions. Moreover, as the difference between predictions obtained by EQL and NL is consistent across a large period interval for the Mj 6.5 event, we hypothesize that there may be other critical issues regarding the accurate representation of modulus reduction and damping behavior for sand dominated stratigraphic profiles (such as in KUMA). This poses a warning in the use of fully nonlinear models, that require a high degree of knowledge of the dynamic properties of the soils that rarely can be obtained in real situations.

Abbreviations

3C	Three components
AMV	Ambient vibration
CC	Cross-correlation
D	Damping
DC	Dispersion curve
EG	Envelope GoF
EHV	Horizontal-to-vertical spectral ratio of earthquake data
EQL	Equivalent-linear
ESG	Effects of surface geology on seismic motion
FAS	Fourier amplitude spectrum
FEG	EG as a function of frequency
f–k	Frequency–wavenumber
FPG	PG as a function of frequency
G/G_0	Normalized shear modulus
GoF	Goodness-of-fit
GRA	Ground response analysis
H/V	Horizontal-to-vertical spectral ratio of AMV
JIVSM	Japan Integrated Velocity Structure Model
MKZ	Modified Kondner–Zelasko constitutive soil model (Matasović and Vucetic, 1993)
MRDF	Modulus reduction and damping pressure-dependent hyperbolic model fitting procedure
MSPAC	Modified spatial autocorrelation
NL	Nonlinear
L	Love
PG	Phase GoF
PGA	Peak ground acceleration
Qp	P-wave quality factor
Qs	S-wave quality factor
R	Rayleigh
Rd	Epicentral distance
Rref	Site-to-reference distance
RTBF	High-resolution Rayleigh-wave three-component beam forming
Sa	Spectral acceleration
SH	Horizontally polarized shear wave
SNR	Signal-to-noise ratio
SPAC	Spatial autocorrelation
SSR	Standard spectral ratio
TEG	EG as a function of time
TF	Time–frequency
TPG	PG as a function of time
TTF	Theoretical transfer function
Vp	P-wave velocity
Vs	Shear-wave velocity

Supplementary Information

The online version contains supplementary material available at https://doi.org/10.1186/s40623-023-01848-x.

Additional file 1: Rotated H/V from AMV data at KUM array stations. Plots of the H/V amplitude as a function of the azimuth of rotated horizontal components on the horizontal plane. Each plot corresponds to a station of the KUM-M array.

Additional file 2: Array processing of AMV data for surface-wave dispersion curve retrieval by Cross-Correlation (CC), Modified Spatial Autocorrelation (MSPAC) and high-resolution Rayleigh Beam Forming (RTBF) methods. Processing details of CC, MSPAC and RTBF with results of each analysis method.

Author contributions

GDG analyzed the data and performed the surface-wave inversion. SH analyzed the data and performed the ground response analysis. MV analyzed the data and performed the cross-correlation analysis. GM and PB analyzed the data and reviewed the text. GDG and SH wrote the main text in the original draft, which was revised by all the authors. All the authors were involved in the conceptualization of the work. All authors read and approved the final manuscript.

Availability of data and materials

The datasets used and/or analyzed during the current study are available from the committee of the ESG6 blind exercise. The dispersion curves, the inverted models and the 1D response analysis are available on request from the authors.

Hailemikael *et al. Earth, Planets and Space*   (2023) 75:105

Page 23 of 25

Declarations

Consent for publication
Not applicable.

Competing interests
The authors declare that they have no competing interests.

Author details
[1]Istituto Nazionale di Geofisica e Vulcanologia, Via di Vigna Murata 605, 00143 Rome, Italy. [2]Istituto Nazionale di Geofisica e Vulcanologia, Viale Francesco Crispi 43-45, 67100 L'Aquila, Italy.

References

Aki K (1957) Space and time spectra of stationary stochastic waves, with special reference to microtremors. Bull Earthq Res Inst 35:415–457

Aki K, Larner KL (1970) Surface motion of a layered medium having an irregular interface due to incident plane SH waves. J Geophys Res 75(5):933–954

Arai H, Tokimatsu K (2004) S-wave velocity profiling by inversion of microtremor H/V spectrum. Bull Seismol Soc Am 94(1):53–63

Asano K, Iwata T (2016) Source rupture processes of the foreshock and mainshock in the 2016 Kumamoto earthquake sequence estimated from the kinematic waveform inversion of strong motion data. Earth Planet Sp 68:147. https://doi.org/10.1186/s40623-016-0519-9

Bard PY, Bouchon M (1985) The two-dimensional resonance of sediment-filled valleys. Bull Seismol Soc Am 75(2):519–541

Bard PY, Cadet H, Endrun B, Hobiger M, Renalier F, Theodulidis N, Ohrnberger M, Fäh D, Sabetta F, Teves-Costa P, Duval AM (2010) From non-invasive site characterization to site amplification: recent advances in the use of ambient vibration measurements. In: Garevski M, Ansal A (eds) Earthquake Engineering in Europe. Springer, Dordrecht, pp 105–123

Bettig B, Bard P-Y, Scherbaum F, Riepl J, Cotton F, Cornou C, Hatzfeld D (2001) Analysis of dense array noise measurements using the modified spatial auto-correlation method (SPAC): application to the Grenoble area. Bollettino Di Geofisica Teorica Ed Applicata 42(3–4):281–304

Beyreuther M, Barsch R, Krischer L, Megies T, Behr Y, Wassermann J (2010) ObsPy: a python toolbox for seismology. Seismol Res Lett 81:530–533

Bielak J, Graves RB, Olsen K, Taborda R, Ramírez-Guzmán L, Day S, Ely G, Roten D, Jordan T, Maechling P, Urbanic J, Cui Y, Juve G (2010) The ShakeOut earthquake scenario: verification of three simulation sets. Geophys J Int 180(1):375–404

Boaga J, Vignoli G, Cassiani G (2011) Shear wave profiles from surface wave inversion: the impact of uncertainty on seismic site response analysis. J Geophys Eng 8(2):162

Boore DM (2004) Can site response be predicted? J Earthq Eng 8(1):1–41

Borcherdt RD (1994) Estimates of site-dependent response spectra for design (methodology and justification). Earthq Spectra 10:617–653

Bordoni P, Milana G, Lucarelli A, Di Giulio G, Hailemikael S, Vassallo M (2023) Is nonlinearity needed to predict the strong ground-motions from the Kumamoto Mj 6.5 and Mj 7.3 mainshocks at KUMA site? (submitted to this issue)

Capon J (1969) (1969) High-resolution frequency-wavenumber spectrum analysis. Proc IEEE 57(8):1408–1418

Chaljub E, Moczo P, Tsuno S, Bard PY, Kristek J, Käser M, Stupazzini M, Kristeková M (2010) Quantitative comparison of four numerical predictions of 3D ground motion in the Grenoble Valley, France. B Seismol Soc Am 100:1427–1455. https://doi.org/10.1785/0120090052

Chaljub E, Maufroy E, Moczo P, Kristek J, Hollender F, Bard PY, Priolo E, Klin P, de Martin F, Zhang ZG, Zhang W, Chen XF (2015) 3-D numerical simulations of earthquake ground motion in sedimentary basins: testing accuracy through stringent models. Geophys J Int 201(1):90–111

Chimoto K, Yamanaka H, Tsuno S, Miyake H, Yamada N (2016) Estimation of shallow S-wave velocity structure using microtremor array exploration at temporary strong motion observation stations for aftershocks of the 2016 Kumamoto earthquake. Earth Planets Space. https://doi.org/10.1186/s40623-016-0581-3

Chimoto K, Yamanaka H, Tsuno S, Matsushima S (2023) Predicted results of the velocity structure at the target site of the blind prediction exercise from microtremors and surface wave method as Step-1, Report of the experiments for the 6th international symposium on effects of surface geology on seismic motion. Earth, Planets and Space. https://doi.org/10.1186/s40623-023-01842-3

Corporation OYO (2020) Kumamoto Eq. Ground Structure Survey. OYO Corporation, Tokyo, p 2020

Daubechies I (1992) Ten Lectures on Wavelets, SIAM. Society for Industrial and Applied Mathematics, Philadelphia

Di Giulio G, Savvaidis A, Ohrnberger M, Wathelet M, Cornou C, Knapmeyer-Endrun B, Renalier F, Theodoulidis N, Bard PY (2012) Exploring the model space and ranking a best class of models in surface wave dispersion inversion: application at European strong-motion sites. Geophysics 77(3):B1147–B1166

Di Giulio G, Ercoli M, Vassallo M, Porreca M (2020) Investigation of the Norcia basin (Central Italy) through ambient vibration measurements and geological surveys. Eng Geol 267:105501

Di Michele F, May J, Pera D, Kastelic V, Carafa M, Smerzini C, Mazzieri I, Rubino B, Antonietti PF, Quarteroni A, Aloisio R, Marcati P (2022) Spectral element numerical simulation of the 2009 L'Aquila earthquake on a detailed reconstructed domain. Geophys J Int 230(1):29–49

Esmaeilzadeh A, Motazedian D, Hunter J (2019) 3D nonlinear ground-motion simulation using a physics-based method for the Kinburn basin. Bull Seismol Soc Am 109(4):1282–1311

Fäh D, Kind F, Giardini D (2003) Inversion of local S-wave velocity structures from average H/V ratios, and their use for the estimation of site-effects. J Seism 7:449–467

Fäh D, Stamm G, Havenith H-B (2008) Analysis of three-component ambient vibration array measurements. Geophys J Int 172(1):199–213

Fäh D, Wathelet M, Kristeková M, Havenith H, Endrun B, Stamm G, Poggi V, Burjanek J, Cornou C Using ellipticity information for site characterisation. NERIES JRA4 Geotechnical Site Characterisation, task B 2. 2009. http://neries-jra4.geopsy.org/D4/D4-Report.pdf. Accessed 06 Feb 2023

Felicetta C, Mascandola C, Spallarossa D, Pacor F, Hailemikael S, Di Giulio G (2021) Quantification of site effects in the Amatrice area (Central Italy): insights from ground-motion recordings of the 2016–2017 seismic sequence. Soil Dyn Earthq Eng 142:106565

Field EH, Jacob KH (1995) A comparison and test of various site-response estimation techniques, including three that are not reference-site dependent. Bull Seismol Soc Am 85(4):1127–1143

Foti S, Comina C, Boiero D, Socco LV (2009) Non uniqueness in surface wave inversion and consequence on seismic site response analyses. Soil Dyn Earthq Eng 29:982–993

Foti S, Lai CG, Rix G (2014) Strobbia C (2014) Surface wave methods for near-surface site characterization. CRC Press, Boca Raton

Galvez P, Ampuero J-P, Dalguer LA, Somala SN, Nissen-Meyer T (2014) Dynamic earthquake rupture modelled with an unstructured 3-D spectral element method applied to the 2011 M9 Tohoku earthquake. Geophys J Int 198(2):1222–1240

Garofalo F, Foti S, Hollender F, Bard P, Cornou C, Cox BR, Ohrnberger M, Sicilia D, Asten M, Di Giulio G, Forbriger T (2016a) InterPACIFIC project: comparison of invasive and non-invasive methods for seismic site characterization. Part I: intra-comparison of surface wave methods. Soil Dyn Earthq Eng 82:222–240

Garofalo F, Foti S, Hollender F, Bard PY, Cornou C, Cox BR, Dechamp A, Ohrnberger M, Perron V, Sicilia D, Teague D (2016b) InterPACIFIC project: Comparison of invasive and non-invasive methods for seismic site characterization. Part II: Inter-comparison between surface-wave and borehole methods. Soil Dyn Earthq Eng 82:241–254

Gosselin JM, Dosso SE, Askan A, Wathelet M, Savvaidis A, Cassidy JF (2022) A review of inverse methods in seismic site characterization. J Seismol 26:781–821. https://doi.org/10.1007/s10950-021-10047-8

Hardin BO, Drnevich VP (1972) Shear modulus and damping in soils: design equations and curves. J Soil Mech Found Div 98(sm7):667–692

Hailemikael *et al. Earth, Planets and Space*   (2023) 75:105

Page 24 of 25

Hashash YMA, Musgrove MI, Harmon JA, Ilhan O, Xing G, Numanoglu O, Groholski DR, Phillips, CA, Park D (2020) DEEPSOIL 7.0, User Manual. Urbana, IL, Board of Trustees of University of Illinois at Urbana-Champaign

Herrmann RB (1987) Surface wave inversion computer programs in seismology. Saint Louis University, Saint Louis, p 4

Hobiger M, Bard PY, Cornou C, Le Bihan N (2009) Single station determination of Rayleigh wave ellipticity by using the random decrement technique (RayDec). Geophys Res Lett 36(14):L14303

Hobiger M, Cornou C, Wathelet M, Di Giulio G, Knapmeyer-Endrun B, Renalier F, Bard PY, Savvaidis A, Hailemikael S, LeBihan N, Ohrnberger M, Theodoulidis M (2013) Ground structure imaging by inversion of Rayleigh wave ellipticity: sensitivity analysis and application European Strong-motionsites. Geophys J Int 192(1):207–229. https://doi.org/10.1093/gji/ggs005

Hobiger M, Bergamo P, Imperatori W, Panzera F, Marrios Lontsi A, Perron V, Michel C, Burjánek J, Fäh D (2021) Site characterization of Swiss strong-motion stations: the benefit of advanced processing algorithms. Bull Seismol Soc Am 111:1713–1739. https://doi.org/10.1785/0120200316

Japan Seismic Hazard Information System, J-SHIS Version2, NIED. 2023. http://www.j-shis.bosai.go.jp/map/?lang=en. Accessed Feb 2023

Kaklamanos J, Bradley BA (2018) Challenges in predicting seismic site response with 1D analyses: conclusions from 114 KiK-net vertical seismometer Arrays challenges in predicting seismic site response with 1D analyses. Bull Seismol Soc Am 108(5A):2816–2838

Kennett BL, Kerry NJ (1979) Seismic waves in stratified half space. Geophys J R Astron Soc 57:557–583

Kim B, Hashash YMA (2013) Site response analysis using downhole array recordings during the March 2011 Tohoku-Oki earthquake and the effect of long-duration ground motions. Earthq Spectra 29:S37-54

Koketsu K, Miyake H, Suzuki H (2012) Japan Integrated Velocity Structure Model Version 1. Proceedings of the 15th World Conference on Earthquake Engineering, Lisbon, Portugal. 12–17, Paper No. 1773.

Konno K, Ohmachi T (1998) Ground-motion characteristics estimated from spectral ratio between horizontal and vertical components of microtremor. Bull Seismol Soc Am 88(1):228–241

Kottke AR, Rathje EM (2008) Technical manual for Strata. Report No.: 2008/10. Pacific earthquake engineering research center. University of California, Berkeley

Kramer LS (1996) Geotechnical earthquake engineering. Upper Saddle River. Prentice-Hall, USA

Kristeková M, Kristek J, Moczo P, Day SM (2006) Misfit criteria for quantitative comparison of seismograms. Bull Seism Soc Am 96:1836–1850

Kristeková M, Kristek J, Moczo P (2009) Time-frequency misfit and goodness-of-fit criteria for quantitative comparison of time signals. Geophys J Int 178:813–825

Maranò S, Fäh D, Lu YM (2014) Sensor placement for the analysis of seismic surface waves: sources of error, design criterion and array design algorithms. Geophys J Int 197(3):1566–1581

Maranò S, Hobiger M, Fäh D (2017) Retrieval of Rayleigh wave ellipticity from ambient vibration recordings. Geophys J Int 209(1):334–352

Marcucci S, Milana G, Hailemikael S, Carlucci G, Cara F, Di Giulio G, Vassallo M (2019) The deep bedrock in Rome, Italy: a new constraint based on passive seismic data analysis. Pure Appl Geophys 176(6):2395–2410

Matasović N, Vucetic M (1993) Cyclic characterization of liquefiable sands. J Geotech Eng 119(1805):22

Ministry of Education, Culture, Sports, Science and Technology of Japan- MEXT Comprehensive research project for the major active faults related to the 2016 Kumamoto earthquake- FY2016 Progress Report. 2016. https://www.jishin.go.jp/main/chousakenkyuu/kumamoto_sogochousa/h28/h28kumamoto_sogochousa_3_2.pdf. Accessed 06 Feb 2023

Molnar S, Sirohey A, Assaf J, Bard PY, Castellaro S, Cornou C, Cox B, Guillier B, Hassani B, Kawase H, Matsushima S (2022) A review of the microtremor horizontal-to-vertical spectral ratio (MHVSR) method. J Seismol. https://doi.org/10.1007/s10950-021-10062-9

Nakamura Y (1989) A method for dynamic characteristics estimation of subsurface using microtremors on the ground surface. Railw Tech Res Inst Q Rep 30(1):25–33

Nogoshi M, Igarashi T (1971) On the amplitude characteristics of microtremor, Part II. J Seism Soc Jpn 24:26–40

Ohori M, Nobata A, Wakamatsu K (2002) A comparison of ESAC and FK methods of estimating phase velocity using arbitrarily shaped microtremor analysis. Bull Seismol Soc Am 92:2323–2332

Okada H (2006) Theory of efficient array observations of microtremors with special reference to the SPAC method. Explor Geophys 37(1):73–85

Phillips C, Hashash YMA (2009) Damping formulation for nonlinear 1D site response analyses. Soil Dyn Earthq Eng 29:1143–1158

Pilz M, Cotton F (2019) Does the one-dimensional assumption hold for site response analysis? A study of seismic site responses and implication for ground motion assessment using KiK-Net strong-motion data. Earthq Spectra 35(2):883–905

Pilz M, Parolai S, Leyton F, Campos J, Zschau J (2009) A comparison of site response techniques using earthquake data and ambient seismic noise analysis in the large urban areas of Santiago de Chile. Geophys J Int 178(2):713–728

Renalier F, Jongmans D, Savvaidis A, Wathelet M, Endrun B, Cornou C (2010) Influence of parameterization on inversion of surface wave dispersion curves and definition of an inversion strategy for sites with a strong Vs contrast. Geophysics 75(6):B197-209

Rollins KM, Evans M, Diehl N, Daily W (1998) Shear modulus and damping relationships for gravels. J Geotech Geoenviron Eng 124(5):396–405

Schnabel PB, Lysmer J, Seed HB (1972) SHAKE: a computer program for earthquake response analysis of horizontally-layered University of California. Earthquake Engineering Research Center, Berkeley

SESAME European project. Guidelines for the implementation of the H/V spectral ratio technique on ambient vibrations measurements, processing and interpretation. Deliverable D23.12. 2005. http://sesame.geopsy.org/Papers/HV_User_Guidelines.pdf

Shapiro NM, Campillo M (2004) Emergence of broadband Rayleigh waves from correlations of the ambient seismic noise. Geophys Res Lett. https://doi.org/10.1029/2004GL019491

Steidl JH, Tumarkin AG, Archuleta RJ (1996) What is a reference site? Bull Seismol Soc Am 86(6):1733–1748

Stewart JP, Afshari K, Hashash YM (2014) Guidelines for performing hazard-consistent one-dimensional ground response analysis for ground motion prediction. Peer Rep 16:117

Tao Y, Rathje E (2020) Taxonomy for evaluating the site-specific applicability of one-dimensional ground response analysis. Soil Dyn Earthq Eng 128:105865

Thompson EM, Baise LG, Tanaka Y, Kayen RE (2012) A taxonomy of site response complexity. Soil Dyn Earthq Eng 41:32–43

Tokimatsu K (1997) Geotechnical site characterisation using surface waves. In: Ishihara (ed). Proc. 1st Intl. Conf. Earthquake Geotechnical Engineering vol 3. Balkema. 1333–1368

Tsuno S, Korenaga M, Okamoto K, Yamanaka H, Chimoto K, Matsushima T (2017) Local site effects in Kumamoto City revealed by the 2016 Kumamoto earthquake. Earth Planets Space 69:37. https://doi.org/10.1186/s40623-017-0622-6

Vassallo M, De Matteis R, Bobbio A, Di Giulio G, Adinolfi GM, Cantore L, Cogliano R, Fodarella A, Maresca R, Pucillo S, Riccio G (2019) Seismic noise cross-correlation in the urban area of Benevento city (Southern Italy). Geophys J Int 217(3):1524–1542

Wathelet M (2008) An improved neighborhood algorithm: parameter conditions and dynamic scaling. Geophys Res Lett 35:L09301

Wathelet M, Jongmans D, Ohrnberger M (2005) Direct inversion of spatial autocorrelation curves with the neighborhood algorithm. Bull Seism Soc Am 95(5):1787–1800

Wathelet M, Jongmans D, Ohrnberger M, Bonnefoy-Claudet S (2008) Array performances for ambient vibrations on a shallow structure and consequences over Vs inversion. J Seismol 12(1):1–19

Wathelet M, Guillier B, Roux P, Cornou C, Ohrnberger M (2018) Rayleigh wave three-component beamforming: signed ellipticity assessment from high-resolution frequency-wavenumber processing of ambient vibration arrays. Geophys J Int 215(1):507–523

Wathelet M, Chatelain JL, Cornou C, Di Giulio G, Guillier B, Ohrnberger M, Savvaidis A (2020) Geopsy: a user-friendly open-source tool set for ambient vibration processing. Seismol Res Lett 91(3):1878–1889

Yamanaka H, Ishida H (1996) Application of genetic algorithms to an inversion of surface-wave dispersion data. Bull Earthq Eng 86:436–444

Hailemikael *et al. Earth, Planets and Space*   *(2023) 75:105*

Page 25 of 25

Yee E, Stewart JP, Tokimatsu K (2013) Elastic and large-strain nonlinear seismic site response from analysis of vertical array recordings. J Geotech Geoenviron Eng 139:1789–1801